

## Secondary motion in three-dimensional branching networks

Abhijit Guha and Kaustav Pradhan

Citation: *Physics of Fluids* **29**, 063602 (2017); doi: 10.1063/1.4984919

View online: <http://dx.doi.org/10.1063/1.4984919>

View Table of Contents: <http://aip.scitation.org/toc/phf/29/6>

Published by the *American Institute of Physics*

---

---



**COMPLETELY  
REDESIGNED!**

*Physics Today* Buyer's Guide  
Search with a purpose.

## Secondary motion in three-dimensional branching networks

Abhijit Guha<sup>a)</sup> and Kaustav Pradhan

*Mechanical Engineering Department, Indian Institute of Technology Kharagpur, Kharagpur 721302, India*

(Received 4 March 2017; accepted 21 May 2017; published online 28 June 2017)

A major aim of the present work is to understand and thoroughly document the generation, the three-dimensional distribution, and the evolution of the secondary motion as the fluid progresses downstream through a branched network. Six generations (G0-G5) of branches (involving 63 straight portions and 31 bifurcation modules) are computed in one go; such computational challenges are rarely taken in the literature. More than  $30 \times 10^6$  computational elements are employed for high precision of computed results and fine quality of the flow visualization diagrams. The study of co-planar vis-à-vis non-planar space-filling configurations establishes a quantitative evaluation of the dependence of the fluid dynamics on the three-dimensional arrangement of the same individual branches. As compared to the secondary motion in a simple curved pipe, three distinctive features, viz., the change of shape and size of the flow-cross-section, the division of non-uniform primary flow in a bifurcation module, and repeated switchover from clockwise to anticlockwise curvature and vice versa in the flow path, make the present situation more complex. It is shown that the straight portions in the network, in general, attenuate the secondary motion, while the three-dimensionally complex bifurcation modules generate secondary motion and may alter the number, arrangement, and structure of vortices. A comprehensive picture of the evolution of quantitative flow visualizations of the secondary motion is achieved by constructing contours of secondary velocity  $|\vec{v}_S|$ , streamwise vorticity  $\omega_S$ , and  $\lambda_2$  iso-surfaces. It is demonstrated, for example, that for in-plane configuration, the vortices on any plane appear in pair (i.e., for each clockwise rotating vortex, there is an otherwise identical anticlockwise vortex), whereas the vortices on a plane for the out-of-plane configuration may be dissimilar, and there may even be an odd number of vortices. We have formulated three new parameters ( $E_{S/P}$ ,  $\delta_{SF}$ , and  $\delta_{Gn}$ ) for a quantitative description of the overall features of the secondary flow field.  $\delta_{SF}$  represents a non-uniformity index of the secondary flow in an individual branch,  $E_{S/P}$  represents the mass-flow-averaged relative kinetic energy of the secondary motion in an individual branch, and  $\delta_{Gn}$  provides a measure of the non-uniformity of the secondary flow between various branches of the same generation  $Gn$ . The repeated enhancement of the secondary kinetic energy in the bifurcation modules is responsible for the occurrence of significant values of  $E_{S/P}$  even in generation G5. For both configurations, it is found that for any bifurcation module, the value of  $E_{S/P}$  is greater in that daughter branch in which the mass-flow rate is greater. Even though the various contour plots of the complex secondary flow structure appear visually very different from one another, the values of  $\delta_{SF}$  are found to lie within a small range ( $0.37 \leq \delta_{SF} \leq 0.66$ ) for the six-generation networks studied. It is shown that  $\delta_{Gn}$  grows as the generation number  $Gn$  increases. It is established that the out-of-plane configuration, in general, creates more secondary kinetic energy (higher  $E_{S/P}$ ), a similar level of non-uniformity in the secondary flow in an individual branch (similar  $\delta_{SF}$ ), and a significantly lower level of non-uniformity in the distribution of secondary motion among various branches of the same generation (much lower  $\delta_{Gn}$ ), as compared to the in-plane arrangement of the same branches. *Published by AIP Publishing.* [<http://dx.doi.org/10.1063/1.4984919>]

### I. INTRODUCTION

A recent paper<sup>1</sup> presents a detailed description of the primary flow field in complex three-dimensional internal passages formed by a dichotomously branching network. The main objective of this paper is to study and understand the physics of the secondary motion of a fluid in such a network which is found in several biological systems, the human

bronchial tree being an important example. A branching network may also be used in future engineered small-scale or micro-systems based on fractal or other geometrical algorithms. (Reference 2 discusses an example of a novel heat exchanger for a hypersonic engine, its bio-inspired design being based on the fish-gill morphology.) This paper adopts a model human bronchial tree for specifying the geometry and dimensions of the computational passages in which the fluid dynamics is studied. The network is constructed by connecting cylindrical straight tubes through bifurcation modules.<sup>1</sup> The flow passages in the bifurcation module are three-dimensionally complex,<sup>1</sup> and the flow paths are curved

<sup>a)</sup> Author to whom correspondence should be addressed: a.guha@mech.iitkgp.ernet.in

giving rise to secondary circulation perpendicular to the primary flow, and hence the overall fluid motion assumes a helical path. Although the basic nature of the secondary motion is similar to that in a simple curved pipe,<sup>3</sup> three distinctive features, viz., the change of shape and size of flow-cross-section, division of the non-uniform primary flow in a bifurcation module, and repeated switchover from clockwise to anticlockwise curvature and vice versa in the flow path, make the present situation more complex. Another complexity arises from the fact that, similar to the previous complementary study,<sup>1</sup> here also we have considered two branching configurations side by side: the most widely studied in-plane configuration in which the centrelines of all generations lie on the same plane, and the 90° out-of-plane configuration in which the centreline of each generation is rotated with respect to its grandmother generation following a systematic methodology to form a space-filling three-dimensional structure. Our aim is to understand and thoroughly document the generation, the three-dimensional distribution and the evolution of the secondary motion as the fluid progresses downstream through a branched network. Six generations of branches (involving 63 straight portions and 31 bifurcation modules) are computed in one go; such computational challenges are rarely taken in the literature. Since accurate capturing of the fine details of the secondary motion is more challenging than capturing the primary flow field, we recomputed the entire flow field through the same three-dimensional geometry of flow passages given in Ref. 1 using a much finer mesh here; more than  $30 \times 10^6$  computational elements are used in this work for solutions in a six-generation network.

The fluid flow field in the human bronchial tree determines the transport and deposition of inhaled particles through inter-phase transport of momentum (and, in some cases, also of mass and energy). The secondary flow may affect such transport and deposition processes by altering the path lines and residence times of particles. The knowledge of particle transport and deposition in the bronchial tree is important for understanding (and perhaps controlling) the causation of certain diseases and for targeted drug delivery. A unified theory for the deposition of particles was formulated by Guha,<sup>4</sup> which applies to various flow regimes and particle sizes (from the nanometer to millimeter). A lucid but comprehensive description of the flow of the fluid and particles in the human bronchial tree is given by Guha.<sup>5</sup>

Before embarking upon a study of the secondary fluid motion in branched networks, it is instructive to consider its development in a simple curved pipe. When the fluid flows through a curved pipe,<sup>6–12</sup> the secondary fluid motion develops in planes perpendicular to the curved central axis of the pipe. A transverse pressure gradient develops that balances the centrifugal force due to the curved trajectory of the fluid, with the pressure being greatest at the outer wall (i.e., the wall where radius of curvature is maximum) and smallest at the inner wall. The axial velocity of the fluid is smaller near the top and bottom walls as compared to the central region owing to viscous effects, while the transverse pressure gradient is approximately equal at the peripheral and central regions (since the contour bands of static pressure appear as vertical strips). Consequently, the fluid is pushed along the

pressure gradient in the low axial velocity regions near the top and bottom walls, while the fluid is pushed in the direction of the centrifugal force in the high axial velocity central region. Thus, the secondary flow is set up such that the fluid near the outer wall moves along the top and bottom walls towards the inner wall of the pipe, and the fluid in the central region moves outwards. The secondary motion is, therefore, characterized by two counter-rotating vortices (called Dean vortices<sup>7,8,12</sup>), one in each half (top and bottom) of the cross section. The combination of this secondary flow with the primary flow results in a double helical motion of the fluid in the pipe with symmetric flow fields in the top and bottom halves. It is worth mentioning here that the outer wall in a curved pipe corresponds to the inner edge of a bifurcation module, and the inner wall in a curved pipe corresponds to the outer edge of a bifurcation module.<sup>1</sup> Henceforth, in this paper, we refer to the inner and outer edges of the bifurcation modules only.

The magnitude of the secondary flow velocity and the nature of the secondary flow structures developed on a cross-sectional plane depend on the flow Reynolds number and the curvature of the flow path. In his pioneering work, Dean<sup>3</sup> found that the flow in curved pipes is governed by an important parameter (now known as the Dean number) given by combining the local Reynolds number with the radius of curvature of the pipe. In a later work,<sup>13</sup> he observed that there exists a critical value of the Dean number ( $De$ ) beyond which secondary flow is generated. Horlock<sup>6</sup> studied the secondary flow characteristics in a pipe having a sinusoidal centreline. He found that although the secondary flow intensity is reduced by the presence of two consecutive opposite bends, the flow field cannot be restored. Barua<sup>14</sup> studied the flow in curved tubes at large values of the Dean number. Talbot and Gong<sup>15</sup> performed experiments on the entry flow in a curved pipe, and reported that the secondary boundary layers formed along the top and bottom walls merge near the inner wall leading to separation.

Experiments have also been performed in simple branched geometries. Zhao and Lieber<sup>16,17</sup> performed experiments on the flow in a single symmetric bifurcation using Laser Doppler Velocimetry (LDV) techniques. They reported the presence of a pair of Dean vortices in the daughter branches for an inspiratory flow<sup>16</sup> and four vortices in an expiratory flow.<sup>17</sup> Evegren *et al.*<sup>18</sup> gave a detailed description of the unsteady secondary flow in a daughter branch after a 90° bifurcation. Leong *et al.*<sup>19</sup> performed an experimental study of the secondary flow in double bifurcation geometry. Fresconi and Prasad<sup>20</sup> conducted experiments on four generations of a symmetric planar model of the human lung under steady and oscillatory flow conditions. They presented the secondary flow field as a function of flow direction, Reynolds number, and position in the network. However, all these studies pertaining to the secondary flow in branched networks are limited to planar models comprising up to four generations of branches. It is to be noted that, in a dichotomously branching network, the number of branches increases with the increasing generation number ( $n$ ) as  $2^n - 1$ . Non-planar geometry creates additional challenges in a systematic study.

The present work is aimed at developing a comprehensive understanding of the secondary flow, consisting of both vortical structures and shearing regions, in both in-plane and out-of-plane configurations of branched networks comprising six generations of branches. The effect of the inlet Reynolds number ( $Re$ ) on the secondary fluid motion is also captured through simulations at various values of  $Re$  with representative results being shown at three values, viz.,  $Re = 400$ ,  $Re = 1000$ , and  $Re = 1600$ . The changes in the secondary flow field across bifurcation modules and straight portions are illustrated through vector plots superposed on the contours of the secondary velocity magnitude. It is shown that streamwise vorticity captures best the fine details of the secondary fluid motion on a cross-sectional plane. The  $\lambda_2$  criterion (based on the existence of a pressure minimum where two eigenvalues of the inverse of the pressure Hessian are negative) has been used as a supplemental method for locating the cores of the vortices, and the iso-surfaces of  $\lambda_2$  have been used to depict the evolution of the vortices in the three-dimensional flow field. Moreover, we have formulated three new scalar parameters for a quantitative description of the overall features of the secondary flow field and its evolution down the generations. It is found that other than the Dean vortices, which are also found in simple curved pipes, there may exist anti-Dean vortices in a branched network. In a Dean vortex, the fluid in the central region of a cross-sectional plane moves from the outer edge to the inner edge of a bifurcation, whereas the opposite movement happens in an anti-Dean vortex. Both Dean and anti-Dean vortices may have clockwise or counter-clockwise rotation.

## II. GEOMETRY OF BRANCHING NETWORK

A three-dimensional model of the bronchial tree network is constructed by successively connecting cylindrical sections representing the bronchial airways of a particular generation with those of the next generation through bifurcation modules. A particular generation in the network is referred here by the symbol  $G_n$ , where the index  $n$  denotes the generation number and progressively takes the integer values 0, 1, 2, etc. The six-generation network considered here therefore consists of generations  $G_0$  to  $G_5$ . The dimensions of the branches considered in this study are shown in Table I. The bifurcation angle (angle between two daughter branches emanating from the same mother branch) is set to  $70^\circ$  for all generations here. Based on the configurationally different arrangement of branches in

TABLE I. Dimensions of the first six generations of the human bronchial tree according to Weibel.<sup>21</sup>

Generation number	Diameter (mm)	Length (mm)
G0 (trachea)	18.00	120.00
G1	12.20	47.60
G2	8.30	19.00
G3	5.60	7.60
G4	4.50	12.70
G5	3.50	10.70

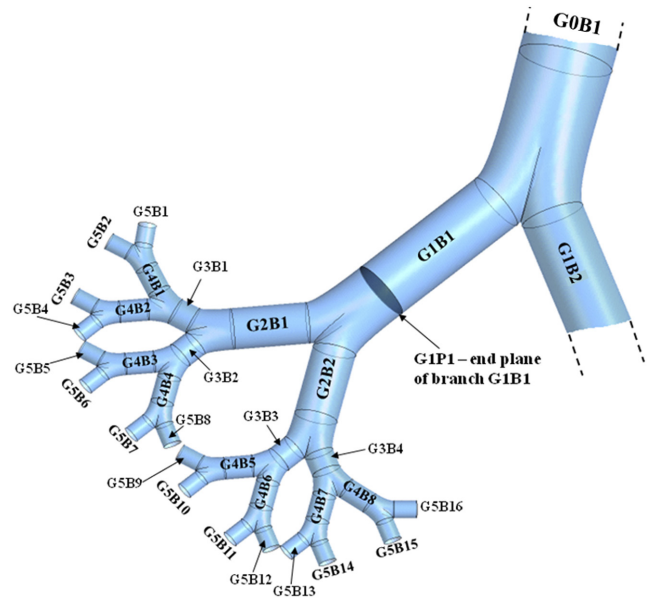


FIG. 1. Six generations ( $G_0$ - $G_5$ ) of a symmetric model of the human bronchial tree; in-plane configuration.

space, two types of networks are considered: in-plane and out-of-plane.

Figure 1 shows a three-dimensional view of the in-plane configuration of a branching network comprising six generations of branches. For the in-plane configuration of the branches, the centerlines of all the bifurcation modules and the cylindrical sections of all generations lie on a single plane (which is denoted by the term “meridional plane”). All the branches are denoted by four characters “ $G_n B_k$ ,” where “ $G_n$ ” denotes the generation to which the branch belongs while “ $B_k$ ” denotes the branch number in a particular generation. Since the present study is concerned with the description of the secondary flow field, the nomenclature of the cross-sectional planes on which the secondary flow field may be described needs to be systematized. The end plane of the branch “ $G_n B_k$ ” is denoted by “ $G_n P_k$ .” As an example, the end plane of branch

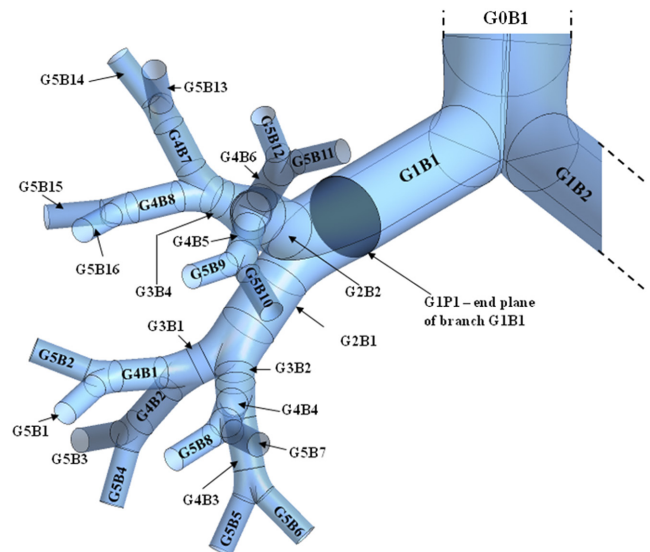


FIG. 2. Six generations ( $G_0$ - $G_5$ ) of a symmetric model of the human bronchial tree; out-of-plane configuration.

G1B1 is denoted by G1P1 (this plane has been highlighted in Fig. 1).

A three-dimensional branching network comprising six generations of branches arranged in the out-of-plane configuration is shown in Fig. 2. Although the dimensions of the branches and the bifurcation angles for this network are the same as those in the in-plane configuration, the planes containing the centrelines of branches of a generation are rotated through  $90^\circ$  with respect to the plane containing the centrelines of their mother and grandmother branches. For a complete description of the three-dimensional arrangement, the reader may refer to Ref. 1. The same nomenclature is used for the branches and cross-sectional planes in the out-of-plane configuration as in the in-plane configuration. However, the complex three-dimensional arrangement of branches makes it difficult to describe how branches belonging to the same generation are numbered. Figure 2 provides a pictorial guide to the system followed for naming the branches in the out-of-plane configuration.

### III. MATHEMATICAL FORMULATION

The present study pertains to a steady, laminar flow of a viscous and incompressible fluid through six generations of a dichotomous branching network. The conservation equations for mass and momentum are given as follows:

$$\nabla \cdot \vec{v} = 0, \quad (1)$$

$$\rho(\vec{v} \cdot \nabla)\vec{v} = -\nabla p + \mu \nabla^2 \vec{v}, \quad (2)$$

where  $\vec{v}$  represents the velocity vector of the fluid,  $\rho$  is the fluid density,  $p$  is the static pressure, and  $\mu$  is the dynamic viscosity of the fluid. In the present set of simulations,  $\rho$  and  $\mu$  are taken as  $1.225 \text{ kg/m}^3$  and  $1.7894 \times 10^{-5} \text{ kg/(ms)}$ , respectively.

In the present study, a uniform velocity is assumed at the inlet to the branching network, the no slip boundary condition is applied on the branch walls, and a pressure boundary condition is used at the ends of the branches of generation G5. The flow in branching networks with curved bifurcation modules, in analogy with the flow in simple curved pipes, is also expected to be governed by the Dean number. However, the complex fashion in which the shape of the cross section changes in the bifurcation modules (thus changing the local curvature) makes it difficult to calculate the local Dean number from the local Reynolds number. In the present study, we therefore consider the parametric variation of the inlet Reynolds number defined as  $Re = 2\rho UR_{G0}/\mu$ , where  $R_{G0}$  is the radius of the branch G0B1.

### IV. COMPUTATIONAL METHOD

The branching geometry is built in SolidWorks,<sup>22</sup> and the meshing and numerical simulation are performed on the ANSYS Workbench<sup>23</sup> using ANSYS Meshing (AM) and FLUENT, respectively. All computations are performed on a Dell Optiplex 9010 computer with an i5-3470 processor.

### A. Mesh generation

The three-dimensional branching network comprising six generations is characterised by gradually decreasing diameters (from 18 mm in the first generation to 3.5 mm in the last generation). A multi-block meshing scheme is adopted here in order to keep the relative size of the computational cells with respect to the branch dimensions approximately constant. ANSYS Meshing (AM) is used for generating the mesh in the three-dimensional bifurcating branches. An unstructured mesh with a sufficiently large number of tetrahedral elements<sup>24</sup> is used in the present study. Boundary layer type meshing (O-grid) is used near the solid walls of the bronchial tubes with sufficiently small thickness of the first layer to accurately capture the gradients near the wall. The number of layers of the boundary layer type mesh is selected such that the height of the last layer is comparable to the size of the neighbouring triangular mesh.

The most critical portion of the geometry from a meshing point of view is the bifurcation module where complex cross-sectional changes take place as the single circular tube transforms into two separate circular tubes.<sup>1</sup> Previous researchers have used both structured and unstructured meshes to obtain the flow field in the 3D branched networks. Studies implementing structured meshes<sup>25</sup> have usually not used any boundary layer type meshing (inflation layers) adjacent to solid walls. Studies using unstructured meshes,<sup>26</sup> on the other hand, have incorporated inflation layers but they suffer from intersection of these inflation layers in the central regions of the bifurcation module. This intersection may be attributed to the fact that the bifurcation module is usually constructed by combining two separate but overlapping narrowing tubes (each connecting the mother branch to one of the daughter branches), and the inflation layers are separately applied to the two narrowing tubes. In the present work, an innovative measure is taken while constructing the geometry so as to ensure that the inflation layers, included to capture the boundary layers, closely follow the shape of the bifurcating walls without any intersection anywhere.

### B. Numerical simulation

The governing equations ((1) and (2)) are solved numerically with the help of the commercial CFD package FLUENT that uses a finite volume technique. The available pressure-based solver is used here. The diffusion terms are discretized using a central difference scheme. A second order upwind scheme is used to discretize the advection terms in the unstructured three-dimensional mesh, so as to reduce the numerical diffusion.<sup>27</sup> A segregated implicit<sup>28</sup> solver is used to solve the resulting system of equations. The solver uses a time-marching technique<sup>29,30</sup> to achieve a steady state solution as the limiting process of an unsteady simulation. The SIMPLE algorithm is used to couple the velocity and pressure for solving the governing equations. Appropriate values of the under-relaxation factors are used such that numerical instabilities are avoided. A convergence criterion of  $10^{-8}$  is used for all the simulations reported in the present work.

The uniform velocity at the inlet to the branching network is specified by using the ‘‘Velocity Inlet’’ boundary

condition feature in FLUENT. Since there is a dearth of knowledge regarding the pressure conditions at the end of the branches of generation G5 in the human bronchial tree, previous researchers<sup>31–33</sup> have resorted to a pressure condition at the end of the branches of the last generation considered. Taking cue from such studies, a pressure boundary condition has been used in the present study using the “Pressure Outlet” boundary condition feature of FLUENT. This feature requires the specification of the gauge static pressure at the outlet boundary, which is then used as a reference to calculate the pressure throughout the computational domain. The gauge static pressure at the outlets is set to zero in the present set of simulations. The CFD simulations determine the change in the static pressure between the inlet and outlet of the network ( $\Delta p_{io}$ ). It is assumed that, for incompressible flow,  $\Delta p_{io}$  does not vary with the absolute value of static pressure specified at the outlet. Thus, once the pressure difference between the inlet and any location in the network is determined from the CFD simulation, the absolute value of static pressure at that location can be calculated from the known value of static pressure at the inlet.

### C. Calculation of velocity and vorticity components

The velocity at any point in the flow domain may be resolved into two mutually perpendicular components: one along the normal to any cross-sectional plane of the branches (primary flow) and the other along the cross-sectional plane (secondary flow). Since all simulation results in FLUENT are generated with respect to a global Cartesian coordinate system (XYZ), and the cross-sectional planes are mostly non-aligned with these axes, the determination of the primary ( $\vec{v}_P$ ) and secondary ( $\vec{v}_S$ ) velocity components is non-trivial. The algorithm used for the determination of the primary and secondary velocity components is summarized below.

Let the unit normal to a cross-sectional plane pointing in the direction of the primary flow be given by

$$\vec{n} = n_X \hat{i} + n_Y \hat{j} + n_Z \hat{k}, \quad (3)$$

where  $\hat{i}$ ,  $\hat{j}$ , and  $\hat{k}$  represent the unit vectors along the X, Y, and Z directions, respectively. The unit normal  $\vec{n}$  points into the cylindrical (straight) portion of a branch at its start-plane and out of the cylindrical portion at its end-plane. Let the velocity vector at that point be given by

$$\vec{v} = u\hat{i} + v\hat{j} + w\hat{k}. \quad (4)$$

The magnitude of the primary velocity is denoted by  $V_P$  and is calculated by taking the component of  $\vec{v}$  along the direction of  $\vec{n}$ ,

$$V_P = \vec{v} \cdot \vec{n} = un_X + vn_Y + wn_Z. \quad (5)$$

The primary velocity vector is therefore given by

$$\vec{v}_P = V_P \vec{n} = V_P n_X \hat{i} + V_P n_Y \hat{j} + V_P n_Z \hat{k}. \quad (6)$$

The secondary velocity is then calculated by the vectorial subtraction of  $\vec{v}_P$  from  $\vec{v}$ . The secondary velocity vector  $\vec{v}_S$  is therefore given by

$$\vec{v}_S = (u - V_P n_X) \hat{i} + (v - V_P n_Y) \hat{j} + (w - V_P n_Z) \hat{k}. \quad (7)$$

The magnitude of the secondary velocity is given by

$$|\vec{v}_S| = \sqrt{(u - V_P n_X)^2 + (v - V_P n_Y)^2 + (w - V_P n_Z)^2}. \quad (8)$$

Two interesting corollaries can be deduced from the above formulation. We note that  $|\vec{v}_S|^2 = |\vec{v}|^2 - |\vec{v}_P|^2 - 2\vec{v}_S \cdot \vec{v}_P = |\vec{v}|^2 - |\vec{v}_P|^2$  since  $\vec{v}_S \cdot \vec{v}_P = 0$  (the two vectors being mutually orthogonal). Second, the condition  $\vec{v}_S \cdot \vec{v}_P = 0$  implies that the six components of the primary and secondary velocity vectors cannot all be positive (or negative) simultaneously (numerical simulations given later are found to satisfy this theoretical constraint).

The secondary fluid motion on a cross-sectional plane may be attributed to a component of vorticity normal to that plane (i.e., in the streamwise direction). Hence, in the present work, an attempt is made to explain the secondary flow patterns on a cross section using the streamwise vorticity parameter,  $\omega_S$ , calculated from the following expression:

$$\omega_S = \vec{\omega} \cdot \vec{n}, \quad (9)$$

where  $\vec{n}$  is the unit normal to that particular plane and  $\vec{\omega}$  is the vorticity vector.

### D. Grid independence study

A comprehensive grid independence study has been performed following the methodology suggested by Roache.<sup>34</sup> A relative error is evaluated according to the following expression:

$$\varepsilon = \left| \frac{\varphi_{i,coarse} - \varphi_{i,fine}}{\varphi_{i,fine}} \right|, \quad (10)$$

where  $\varphi$  represents any flow variable. Here, the secondary velocity magnitude  $|\vec{v}_S|$  is considered for calculating the relative error. The root-mean-square value of the relative error ( $\varepsilon_{rms}$ ) is calculated over a sufficiently large number of points. For this purpose, about 1000 points are considered on each of the five selected cross-sectional planes. Of these five selected planes, three are end planes of branches G0B1, G1B1 and G2B2, and the remaining two planes are taken within the bifurcation modules connecting G0-G1 and G1-G2 branches. On each plane, about 1000 points are chosen along two mutually perpendicular diameters (one lying on the meridional plane and the other containing the trace of the downstream bifurcation ridge). Thus the calculation of the root-mean-square value of the relative error ( $\varepsilon_{rms}$ ) is based on about 5000 points. This  $\varepsilon_{rms}$  is used to provide a scalar measure of grid convergence. Since grid halving (i.e., decreasing the grid size by a factor of 2) is not a trivial task in a three dimensional computational domain, a grid convergence index ( $GCI$ ) was introduced in Ref. 34, which is defined for the refined mesh by the following expression:

$$GCI_{fine} = F_s \frac{\varepsilon_{rms}}{r_{grid}^q - 1}. \quad (11)$$

Here,  $q$  is the order of discretization of all terms in space,  $F_s$  is the factor of safety, and  $r_{grid}$  is the grid refinement factor defined as  $r_{grid} = (N_{fine}/N_{coarse})^{1/3}$ , where  $N$  is the number of elements in the mesh. The value of  $F_s$  is set to 3, such that the  $GCI$  value represents a scaled version of  $\varepsilon_{rms}$  for values of  $r_{grid} \neq 2$ . The two values each of  $\varepsilon_{rms}$  and  $r_{grid}$ , for the two sets of three meshes (coarse, medium, and fine; medium, fine, and very fine) used for establishing grid independence, are used to iteratively find a value of  $q$ . The closer the value of  $q$  comes to its original value (i.e.,  $q = 2$  for the adopted

TABLE II. Details of the grid independence study for the in-plane configuration of branching network comprising generations G0-G5 performed at  $Re = 1000$ .

Number of elements in mesh	$r_{grid}$	$\epsilon_{rms}$	$GCI$
542 115 (coarse)-1 838 556 (medium)	1.502	0.045	0.107
1 838 556 (medium)-6 384 237 (fine)	1.514	0.018	0.041
6 384 237 (fine)-30 942 837 (very fine)	1.692	0.017	0.027

second-order spatial discretization), the better is the grid independence.

The details of the meshes with results of the grid independence test for the in-plane configuration of the symmetric bronchial tree model are tabulated in Table II. The value of  $q$  is calculated to be 1.91 for the two sets of three meshes (coarse, medium, and fine; medium, fine, and very fine). Considering the grid independence data presented in Table II, the fine mesh would give an acceptable result. However, for increased precision of the CFD results and for increased smoothness, with finer details, of the various contours presented later in Sec. V, we have used the “very fine” mesh with 30 942 837 computational elements for all subsequent simulations for the in-plane configuration.

The details of the similar procedure followed for establishing the grid independence of the solutions for the out-of-plane configuration are given in Table III. The value of  $q$  is calculated to be 2.08 for the two sets of three meshes (coarse, medium, and fine; medium, fine, and very fine). Although the “fine” mesh would have been considered adequate on the basis of the grid independence data alone (Table III), the “very fine” mesh with 31 229 470 computational elements is used for all subsequent simulations for the out-of-plane configuration, for the above-mentioned reasons of improved precision of computed results and quality of the flow visualization diagrams.

### E. Validation of computational results

The present numerical method has been validated by comparing the results obtained by the present method with the experimental results of Fresconi and Prasad.<sup>20</sup> They performed experiments to determine the secondary flow field in a symmetric in-plane configuration of branching network comprising four generations. They presented the average value of the steady-state secondary velocity normalized by the average primary velocity as a function of the local Reynolds number and distance downstream of a bifurcation ridge. In our numerical work, we replicated their geometry in which the diameter of the G0 branch is 1.28 cm, the diameter reduction ratio is 0.78, the length to diameter ratio is 3.5, and the bifurcation

TABLE III. Details of the grid independence study for the out-of-plane configuration of branching network comprising generations G0-G5 performed at  $Re = 1000$ .

Number of elements in mesh	$r_{grid}$	$\epsilon_{rms}$	$GCI$
578 895 (coarse)-1 838 753 (medium)	1.470	0.047	0.121
1 838 753 (medium)-6 325 677 (fine)	1.510	0.021	0.048
6 325 677 (fine)-31 229 470 (very fine)	1.703	0.020	0.031

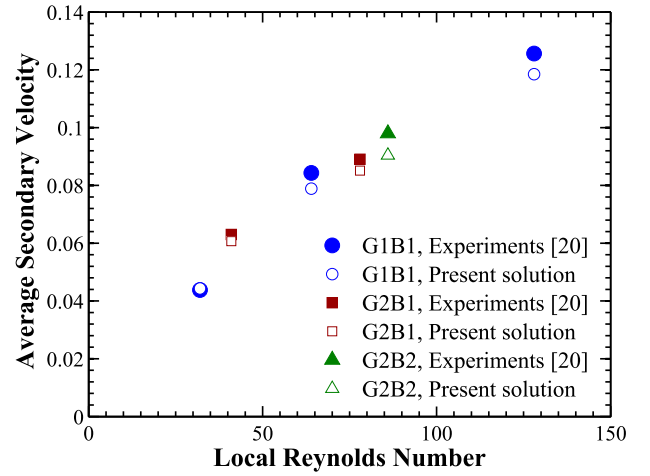


FIG. 3. Comparison of the present numerical results with previous experimental results for a symmetric four generation in-plane branching network.

angle is  $70^\circ$ . Figure 3 shows a comparison of the average secondary velocity (normalized by the average primary velocity) obtained by the present numerical method with the experimental results of Ref. 20. The secondary velocities are compared in branches G1B1, G2B1, and G2B2 at cross-sectional planes that are located at a distance equal to one diameter (of that branch) downstream of the point of intersection of its centreline with that of its mother branch and sister branch. The good agreement of the present results with the experimental results lends confidence in the results reported in the present paper pertaining to networks comprising six generations of branches.

## V. RESULTS AND DISCUSSION

The flow in symmetric dichotomous branching networks is characterized by asymmetric mass-flow distribution<sup>1</sup> and complex secondary flows. The secondary flow in the daughter branches in a two-generation network (comprising a single bifurcation module) shows features similar to that in a curved pipe,<sup>3</sup> with two counter-rotating vortices in the cross section. In the present work, we investigate the generation, the three-dimensional distribution, and the evolution of secondary motion as the fluid progresses downstream through a branched network comprising six generations of branches. By considering both the in-plane and out-of-plane configurations, we establish the effect of the configurationally different arrangement of the branches on the secondary flow field.

It was established in Ref. 1 that in spite of the asymmetry in the flow field developed in a symmetric branching network (as used here) due to the effects of inertia and flow path curvature, there exists a certain systematic order that makes it possible to ascertain the flow field in all branches of a particular generation by determining the flow field in some systematically selected branches of that generation. Subsequently, it was shown that it is necessary and sufficient to determine the flow field in the branches lying on one side of the longitudinal symmetry plane for the in-plane configuration. Similarly, it is necessary and sufficient to determine the flow field in branches lying

in one quarter of the network for the out-of-plane configuration. In the course of the present work, it is found that exactly the same conclusion holds true also regarding the secondary velocity field. Hence, this paper discusses the secondary flow field in half of the network for the in-plane configuration and that in a quarter of the network for the out-of-plane configuration.

### A. Analysis of secondary motion for in-plane configuration

It is to be realised that although the centrelines of all branches lie on a single plane in the in-plane configuration, the internal flow passages are three-dimensional and vary in a complex manner in the flow direction. This gives rise to complex secondary flow fields in the branches of the G0-G5 network. In Sec. V A 1, the general features of the secondary flow field are illustrated through vectors of secondary velocity superposed on the contours of secondary velocity magnitude  $|\vec{v}_s|$  at the start-planes and end-planes of selected branches. Section V A 2 shows the three-dimensional modification of the secondary flow field in the complex internal passages of a bifurcation module. In Sec. V A 3, the secondary flow patterns on a cross-sectional plane are correlated to a scalar parameter. The evolution of the secondary flow field in the G0-G5 network is demonstrated in Sec. V A 4 through contour plots and newly defined scalar parameters.

#### 1. General features of the secondary flow field

The development of a secondary motion perpendicular to the main flow due to a curved flow path was explained in Sec. I. In a branching network, the curvature of the flow path in the bifurcation module gives rise to a similar secondary flow field. However, there are additional complexities associated with the secondary flow in a branching network. First of these is the complex fashion in which the cross section changes from a circle of diameter equal to that of the mother branch to two separate circles with diameters equal to that of the daughter branches.<sup>1</sup> Second, a secondary fluid motion towards the outer edges of the bifurcation is generated by the presence of the bifurcation ridge and flow division into the daughter branches. Third, the non-uniform velocity distribution at the inlet plane of a bifurcation module downstream of generation G1 leads to different secondary flow structures in the two daughter branches. Finally, the repeated switchover from clockwise to anticlockwise curvature and vice versa in the flow path considerably affect the secondary flow field.

In Fig. 4, we present the vectors of secondary velocity superposed on the contours of secondary velocity magnitude  $|\vec{v}_s|$  at selected cross-sectional planes for  $Re = 400$ . The selection of the cross-sectional planes is such that the changes in the secondary flow field across a bifurcation module and that across the straight portion of a branch may be separately established. Stations (a) and (b) in Fig. 4 correspond to the start-plane and end-plane of branch G1B1, stations (c) and (d) correspond to the start-plane and end-plane of branch G2B1, and stations (e) and (f) correspond to the start-plane and end-plane of branch G2B2. The representational convention is selected such that the primary flow is towards the reader

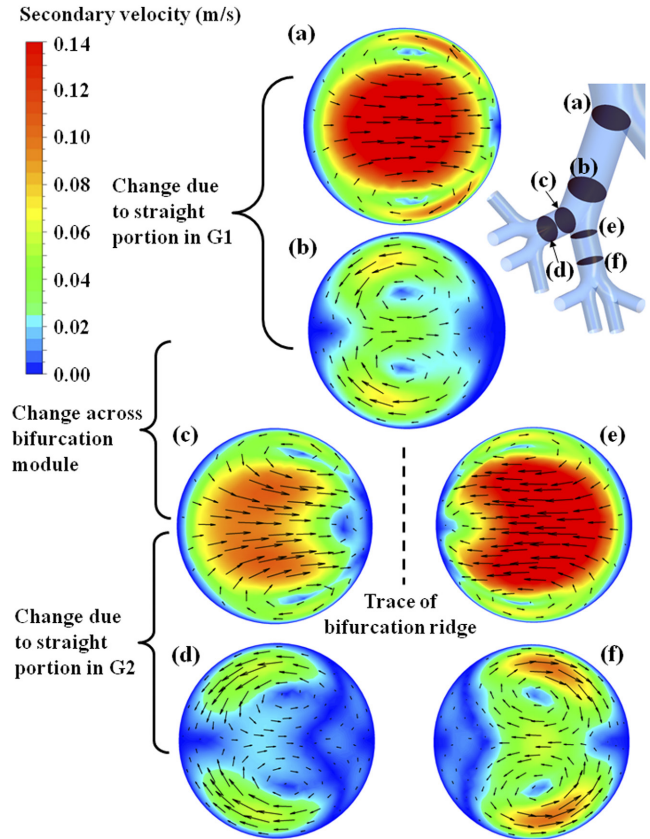


FIG. 4. Secondary velocity vectors superposed on the contours of secondary velocity magnitude on the start-planes and end-planes of branches G1B1, G2B1, and G2B2 for  $Re = 400$ ; in-plane configuration. (The length of the vectors on any cross-sectional plane indicates the secondary velocity scaled by the respective maximum secondary velocity on that plane. Contour plots are represented in circular areas of equal size to keep clarity in the flow features in branches of smaller diameters.)

with the trace of the bifurcation ridge indicating its actual position and orientation with respect to the cross-sectional planes shown in the figure. Figure 4 shows that the secondary flow field is symmetric about a horizontal line in the diagram (representing the “meridional plane”); this feature is analogous to the same symmetry established for the primary flow in Ref. 1.

With the fluid having traversed a single bifurcation module up to the start-plane of G1B1, the secondary flow pattern at station (a) is similar to that in a simple curved pipe.<sup>3</sup> As the fluid travels along the straight portion of branch G1B1, the magnitude of the secondary velocity decreases considerably and the locations of the maximum secondary velocity tend to shift from a central region to near the top and bottom walls. The cores of the Dean vortices,<sup>12</sup> on the other hand, tend to shift from the peripheral regions on the start-plane to more central regions on the end-plane of branch G1B1 [station (b)]. Similar changes in the secondary flow pattern are also found to occur across the straight portions of branches G2B1 [stations (c) and (d)] and G2B2 [stations (e) and (f)]. In spite of these changes, the basic flow structure (i.e., number of vortices and sense of rotation in the vortices) remains unaltered across the straight portion of a branch. For example, the Dean type flow developed at stations (c) and (e) are retained, respectively, at stations (d) and (f) for  $Re = 400$  (Fig. 4).

Figure 4 also establishes the changes in the secondary flow pattern that occur across a bifurcation module. While station (b) corresponds to the start of the bifurcation module connecting G1B1, G2B1, and G2B2, stations (c) and (e) correspond to the end of the same module. Three changes in the secondary flow that are observed to occur across the bifurcation module are as follows: (i) a significant increase in the maximum value of the secondary velocity, (ii) a shift of this maximum towards the central regions of the cross sections of the daughter branches, and (iii) a shift of the Dean vortices towards the top and bottom walls. While the introduction of a fresh secondary motion in the curved bifurcation module is responsible for the increased secondary velocity, the shifting of the vortices may be attributed to the changing cross-sectional shape and size in the bifurcation module. The secondary flow pattern at station (e) shows the same qualitative features as those at station (c). However, the sense of rotation of the fluid in the top half of the cross section at station (e) is opposite to that at station (c). This may be attributed to the opposite curvatures along the flow paths leading to stations (c) and (e). Thus, it is inferred that the effect of local curvature of the flow path dominates over the effect of upstream flow history. A comparison of the contours of secondary velocity magnitude at stations (c) and (e) shows that the maximum (and average) value of the secondary velocity is greater at station (e) than that at station (c). This is in line with the conclusion regarding mass-flow distribution in the branches of generation G2.<sup>1</sup>

The general features of the secondary flow described in Fig. 4 are found to hold good throughout the branching network for  $Re = 400$ . However, computations at various higher values of inlet Reynolds number showed that for  $Re \geq 1000$ , deviations from these general features occur at certain locations. A representative flow solution of this class is shown in Fig. 5 at  $Re = 1000$ . The stations (a)-(f) in Fig. 5 are the same as those in Fig. 4. A second pair of vortices develops in the central region near the inner edge of the bifurcation module at station (c) for the higher  $Re$  flow giving rise to a four-vortex system. The sense of rotation of the fluid in these newly formed vortices is opposite to that in a typical Dean vortex.<sup>11</sup> Hence, these are referred to as anti-Dean vortices. The formation of the anti-Dean vortices was attributed to the double-peaked (M-shaped) velocity profile (about the diameter which contains the trace of the bifurcation ridge) in the preceding mother branch.<sup>19</sup> The development of the second pair of vortices can also be thought of as a result of the interaction of two secondary flow streams: (i) a stream of fluid travelling towards the inner edge of the bifurcation due to centrifugal effects and (ii) a stream travelling toward the outer edge of the bifurcation generated due to the presence of the bifurcation ridge.

The changes in the secondary flow field across the straight portion of a branch that was observed in Fig. 4 (i.e., attenuation of secondary velocity and a shift in the position of vortices) also holds good for  $Re = 1000$  (Fig. 5). It is to be noted that although the four-vortex system becomes more clearly visible at the end-planes of the branches [stations (d) and (f) in Fig. 5], the magnitude of the secondary velocity is considerably smaller on the end-planes as compared to that

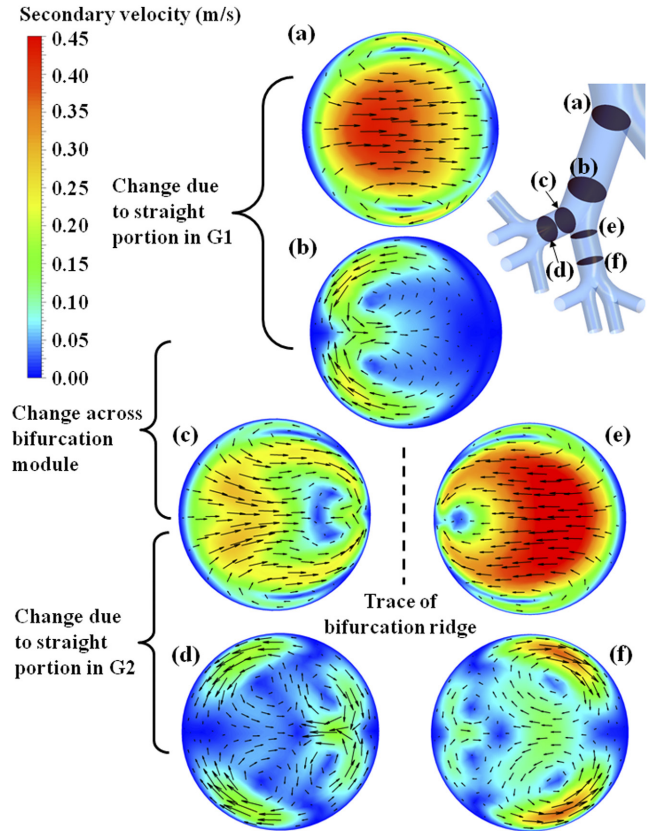


FIG. 5. Secondary velocity vectors superposed on the contours of secondary velocity magnitude on the start-planes and end-planes of branches G1B1, G2B1, and G2B2 for  $Re = 1000$ ; in-plane configuration. (The length of the vectors on any cross-sectional plane indicates the secondary velocity scaled by the respective maximum secondary velocity on that plane.)

on the start-planes of G2B1 and G2B2 [stations (c) and (e) respectively].

A comparison of Figs. 4 and 5 shows that the secondary velocity magnitude on any of the cross-sectional planes shown in the figures increases with an increase in the inlet Reynolds number from 400 to 1000 (this trend is also seen to exist for computations performed up to  $Re = 1600$ ). A general observation that can be made from Figs. 4 and 5 is that the centres of all the vortices (Dean or anti-Dean) usually correspond to regions of low secondary velocity. Since it is known that the flow field is symmetric about a horizontal line in the diagram, only those regions of low secondary velocity (surrounded by higher secondary velocities) correspond to vortices, which occur symmetrically in both the top and bottom halves of the cross section. However, it is difficult to correlate the complete secondary flow structures with the contours of secondary velocity magnitude.

## 2. Three-dimensional modification of the secondary flow field in the complex internal passages of a bifurcation module

For dichotomous branching, a bifurcation module connects the end of a cylindrical section (representing the “mother” branch for this module) to the beginning of two cylindrical sections (representing the “daughter” branches). The cross-sectional shape of the bifurcation module is circular at the beginning at station (a) (Fig. 6) so that it can seamlessly

merge with the cylindrical section of the preceding (mother) branch. Then the shape changes in a complex fashion,<sup>1</sup> as shown in the figure at stations (b)–(d), finally being circular again at stations (e) and (f) in order to seamlessly merge with the two cylindrical sections of the next generation (daughter branches). Thus, even for the in-plane configuration where the centrelines of all cylindrical sections and bifurcation modules lie on a single plane (the “meridional plane”), the internal flow passages are three-dimensional and vary in a complex manner in the flow direction. There is no analogue of this complexity in the usual description of the secondary motion in curved pipes.

An important criterion for capturing the secondary motion properly is that the planes ought to be constructed such that there is no component of the primary motion along that plane (a few previous studies, e.g., Refs. 25 and 35, of the secondary motion in bifurcating geometries suffer from non-compliance of this critical principle). The orientations of the appropriate cross sections would change along the pathline and may even be non-planar (i.e., curved surfaces) if the local curvatures of the bounding walls are different at different points (the exact values of which are not digitally known from the solid modelling software used to create the bifurcating geometry). We therefore have developed a simple method of constructing appropriate planes that is practically implementable and gives results with sufficient accuracy. The method is described next.

Figure 6 shows how the complex internal passages of a bifurcation module modify the secondary flow field. The bifurcation module connecting the branches G0B1, G1B1, and G1B2 is selected for the above purpose. Station (a) corresponds to the end-plane of G0B1 (i.e., the start-plane of the bifurcation module). Station (c) corresponds to the cross-sectional plane passing through the point of intersection of

the centrelines of G0B1, G1B1, and G1B2 and with normal along the centreline of G0B1. Station (b) is located midway between stations (a) and (c). Stations (e) and (f) correspond to the start-planes of G1B1 and G1B2, respectively. The fluid stream is divided in the bifurcation module and each of the two newly formed streams is diverted through an angle of  $35^\circ$  (half of the bifurcation angle) with respect to the centreline of G0B1, across the bifurcation module. It is assumed here that this diversion of the flow path is restricted to the region between stations (c) and (e) [or (f)] and that the diversion angle varies linearly with distance from station (c) (along the centreline of G0B1). Accordingly, station (d) is defined at that location where the flow path has been diverted through  $17.5^\circ$  with respect to the centreline of G0B1. The cross section at station (d) consists of two planes (which subtend an angle of  $145^\circ$  on the upstream side) intersecting along a line which coincides with the trace of the bifurcation ridge at station (d).

It is observed in Fig. 6 that the secondary velocity magnitude  $|\vec{v}_s|$  at stations (a) and (b) is small, with the secondary motion directing the fluid from peripheral regions towards the centre of the cross section. At station (c), the magnitude of the secondary velocity is much greater than that at the previous station, and the secondary flow vectors show a distinct motion of fluid towards the outer edge of the bifurcation. This motion of the fluid may be attributed to the combined effects of the gradual flattening of the cross section in the bifurcation module and the presence of the downstream bifurcation ridge. At station (d), there is a reversal in the direction of the secondary fluid motion, and the vectors show that the fluid is driven towards the centreline. This indicates that the centrifugal effects due to the curvature of the flow path dominate over the other effects governing the secondary fluid motion. Moreover, the magnitude of the secondary velocity at station

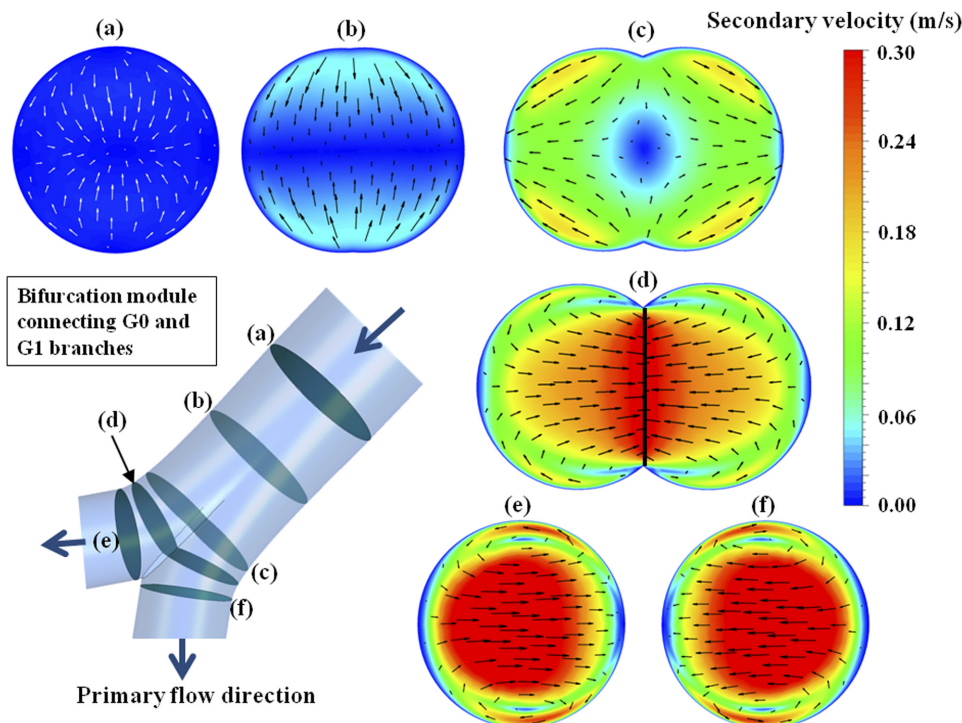


FIG. 6. Changes in the secondary flow field in the complex internal passage in the bifurcation module connecting G0 and G1 branches for  $Re = 1000$ ; in-plane configuration. (The representational convention is selected such that the trace of the bifurcation ridge appears as a vertical line in the diagram and the primary flow is towards the reader.)

(d) is also greater than that at station (c). The secondary flow patterns at stations (e) and (f) are similar to that observed for a simple curved pipe (i.e., Dean type flow). The shift in the position of the maximum secondary velocity away from the inner edges of the bifurcation at these stations as compared to station (d) may be attributed to the region of low velocities developed in the vicinity of the bifurcation ridge due to viscous effects.

The bifurcation module is therefore responsible for a significant increase in secondary velocities [comparing the velocities at stations (a), (e), and (f)], as well as the development of new secondary flow structures (Dean vortices formed at the end of the bifurcation module that were absent at its inlet plane). However, the same bifurcation module preserves certain symmetry present at its inlet plane. The secondary flow at station (a) is symmetric about a horizontal line (meridional plane) as well as about a vertical line (trace of the bifurcation ridge). The preservation of symmetry about the horizontal line is observed in the secondary velocity contours at stations (e) and (f). The symmetry about the vertical line manifests itself in the development of identical (mirror images) secondary flow structures in the two daughter branches [stations (e) and (f)].

### 3. Finding which other flow variable correlates with secondary flow pattern

A study is undertaken to determine whether the secondary flow structures on a cross-sectional plane can be correlated with any flow variable. Superposition of the secondary velocity vectors on contours of primary velocity magnitude ( $|\vec{v}_p|$ ) and total pressure showed that there exists no definite correlation between the secondary flow pattern and these variables (those diagrams have not been included here for brevity). The secondary velocity vectors superposed on the contours of secondary velocity magnitude  $|\vec{v}_s|$  (see Figs. 4–6) show that the vortex cores correspond to the regions of low secondary velocities which are surrounded by the regions of greater secondary velocities. However, the complete secondary flow pattern including the direction of rotation of the fluid in the vortices and other flow features (such as the secondary boundary layer<sup>11</sup>) could not be captured by the contours of  $|\vec{v}_s|$ .

Since the secondary fluid motion on a cross-sectional plane may be attributed to a component of vorticity normal to that plane, it was anticipated that the streamwise vorticity parameter  $\omega_S$  [defined in Eq. (9)] may correlate with the secondary flow structures. Figure 7 shows the secondary velocity vectors superposed on the contours of  $\omega_S$  (scaled by its maximum value on that plane) on the end-planes of branches G1B1 and G2B2. The representational convention adopted in Fig. 7 is the same as that used in Figs. 4–6. The colour map is selected such that both blue and red indicate regions of high streamwise vorticity but of opposite sign; blue represents a high negative value of  $\omega_S$  associated with a clockwise rotation of the fluid, while red represents a high positive value of  $\omega_S$  associated with an anti-clockwise rotation of the fluid. The secondary velocity vectors in Fig. 7 show that the contours of streamwise vorticity beautifully capture the qualitative features of the secondary flow pattern. A vortex is represented by a region of high  $\omega_S$  in the cross section, separated from the wall by another region of high  $\omega_S$  (but of opposite sign). The region of high  $\omega_S$  adjacent to the wall corresponds to a secondary boundary layer in the cross section.<sup>11</sup> It is well known that the vorticity in a two-dimensional boundary layer varies from a maximum value at the wall to zero at the edge of the boundary layer. This variation of the vorticity can be observed in Fig. 7, where  $\omega_S$  varies from a high value at the walls to zero at some distance from the wall where the secondary boundary layer merges with the vortex. Our finding of a direct correspondence between the contours of streamwise vorticity parameter and the pattern of secondary velocity vectors for flow in bifurcating networks is in line with the findings of Hawthorne<sup>7</sup> in the context of the flow in a curved pipe regarding how the secondary circulation gives rise to a component of vorticity in the streamwise direction. (It is to be appreciated that the contours of streamwise vorticity are indicative of the pattern of the secondary velocity vectors and not of the contours of secondary velocity magnitude; this subtle point will be clearer in Sec. V A 4.)

It was shown in Fig. 4 that the secondary flow field on the plane G1P1 is qualitatively similar to that in a curved pipe. Such a flow field is characterized by the presence of two similar

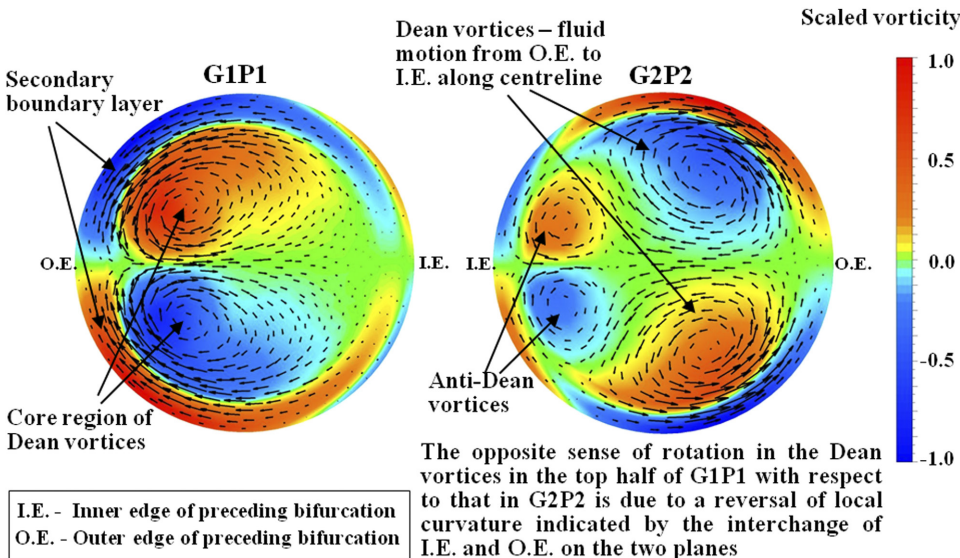


FIG. 7. Secondary velocity vectors superposed on the contours of streamwise vorticity  $\omega_S$  on planes G1P1 and G2P2 for  $Re = 1000$ ; in-plane configuration. ( $\omega_S$  is scaled by its maximum value on that plane. G1P1 and G2P2 are the end-planes of the branches G1B1 and G2B2 respectively.)

counter-rotating vortices, one in each half of the cross section and secondary boundary layers between the vortices and the walls in the respective halves. The pattern of secondary velocity vectors on the plane G1P1 in Fig. 7 shows that the fluid enters this boundary layer (indicated by the blue region near the top wall) near the inner edge (I.E.) of the bifurcation and leaves it near the outer edge of the bifurcation (O.E.). The red coloured region in the top half of the cross section represents a Dean vortex with anticlockwise fluid rotation. Thus the overall secondary fluid motion in the top half of G1P1 is such that fluid moves from O.E. to I.E. along the central regions of the cross section (due to centrifugal effects) and along the top and bottom walls towards O.E. (due to pressure gradient). The symmetry in the secondary flow field about the meridional plane (horizontal centreline in the diagram) is also captured by the contours of  $\omega_S$  which show exactly the same secondary flow structures in the bottom half of G1P1, but of opposite sense (a blue coloured vortex and a red coloured boundary layer).

The secondary flow pattern on the plane G2P2 for  $Re = 1000$  is also shown in Fig. 7. It was observed in Fig. 5 that two pairs of vortices (one pair of Dean type and the other pair of anti-Dean type) develop on this plane and that the secondary flow pattern is symmetric about a horizontal centreline in the diagram. These features are accurately captured by the contours of  $\omega_S$  shown in Fig. 7. Since a pair of vortices appear in the top half of G2P2, it is important to correctly identify the Dean vortex from the anti-Dean vortex. A Dean vortex is formed by the motion of fluid towards I.E. along the centreline and towards O.E. along the top and bottom walls. Thus, the vortex in blue colour in the top half represents the Dean vortex,

and hence the vortex in red colour in the same half of the cross section represents the anti-Dean vortex (of opposite sense to that of the Dean vortex). Figure 7 also shows that there occur two pairs of secondary boundary layers on plane G2P2, each one associated with one of the four vortices. Moreover, fluid enters these boundary layers near the top and bottom walls. This is quite different from the secondary boundary layer flow observed in the presence of only two vortices (e.g., on plane G1P1). Figure 7 shows that the streamwise vorticity parameter  $\omega_S$  not only conveys the sense of rotation in a vortex through a change of sign, but also captures the secondary boundary layer.

#### 4. Evolution of secondary flow for in-plane configuration

In Secs. V A 1–V A 3, we have discussed the general features of the secondary flow field in a branched network and its variation with the inlet Reynolds number. Another important aspect that requires investigation is the spatial evolution of the secondary flow as the fluid travels down the generations from G0 to G5. Other than providing a comprehensive picture of the evolution of quantitative flow visualizations of secondary motion (e.g., contours of  $|\vec{v}_S|$ ,  $\omega_S$  and  $\lambda_2$ ), we have formulated new parameters ( $E_{S/P}$ ,  $\delta_{SF}$ , and  $\delta_{GN}$ ) for a quantitative description of the overall features of the secondary flow field.

Figure 8 shows the contours of secondary velocity magnitude  $|\vec{v}_S|$  on the end-planes of the branches of generations G1 to G3 at  $Re = 1000$ . The stations (a)–(g) at which the contour plots are presented are shown in the schematic diagram within Fig. 8. As expected for this configuration, the secondary velocity field

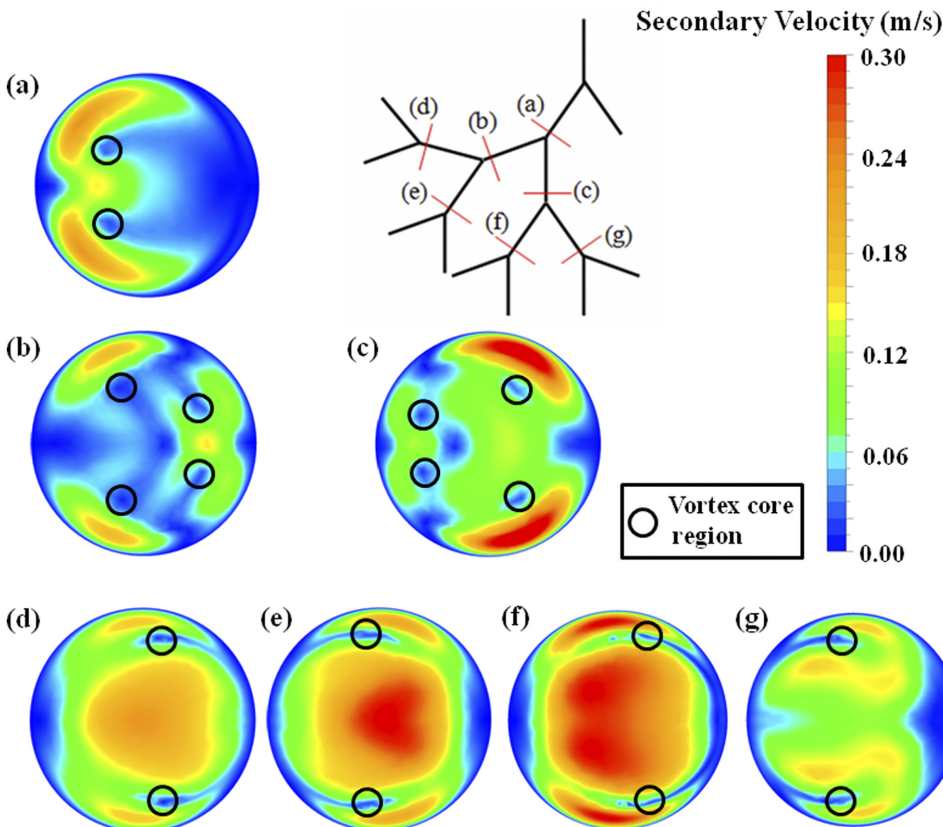


FIG. 8. Contours of secondary velocity magnitude at the end-planes of branches of generations G1–G3 for  $Re = 1000$ ; in-plane configuration. (The representational convention is set such that the downstream bifurcation ridge appears as a vertical line in the diagram and the primary flow is towards the reader.)

is symmetric about a horizontal centreline in the diagram (i.e., the trace of the meridional plane).

In the present study, the  $\lambda_2$ -criterion<sup>36</sup> has been used as a supplemental method for locating the cores of the vortices in the flow field (denoted by small circles in Fig. 8, where the secondary velocity is usually low). According to this criterion, any point in the flow field, for which  $\lambda_2 < 0$ , is part of a vortex. Here,  $\lambda_2$  refers to the median eigenvalue of the symmetric tensor  $S^2 + \Omega^2$ , where  $S$  is the symmetric part and  $\Omega$  is the anti-symmetric part of the velocity gradient tensor. It is observed in Fig. 8 that the secondary flow at plane G1P1 [station (a)] is characterized by a pair of similar vortices, one in each half of the cross section. The planes G2P1 and G2P2 [i.e., stations (b) and (c)] are marked by the presence of two pairs of vortices. The end-planes of the G3 branches [stations (d)-(g)] are again characterized by a single pair of vortices.

Next we turn our attention to the magnitude of secondary velocity displayed in Fig. 8. It is observed that the maximum (and average) secondary velocity on plane G2P2 is greater than that on plane G2P1. It was established in Ref. 1 that the mass-flow rate in branch G2B2 is greater than that in branch G2B1 due to the combined effects of the flow path curvature and inertia. It is also observed that in generation G3, the average secondary velocity is maximum on the end-plane of branch G3B3 [station (f)], the same branch that was found to have the maximum mass-flow rate among all the G3 branches.<sup>1</sup> Thus, the connection is established here that the secondary velocity is greater at the end-plane of that branch which has a higher mass-flow rate.

It was shown in Figs. 4 and 5 that, at the start of the straight portion of a branch, the maximum secondary velocity generally occurs at central locations on the cross section and

has the general tendency to shift towards the top and bottom walls as the flow progresses to the end plane of that branch. This shifting is complete in planes G1P1, G2P1, and G2P2, while the shift is partial on the end-planes of the branches of G3 [stations (d)-(g)], as shown in Fig. 8, for short lengths of the branches of this generation.

The physical significance of the streamwise vorticity parameter  $\omega_S$  in the description of secondary motion in branched networks was demonstrated in Fig. 7. Accordingly, Fig. 9 shows the spatial evolution of  $\omega_S$  in the branched network for  $Re = 1000$ . The schematic diagram within the figure shows the locations of the cross-sectional planes in generations G1-G3 [stations (a)-(g)] on which the contours of  $\omega_S$  are plotted. The contours of  $\omega_S$ , like the contours of  $|\vec{v}_S|$ , are symmetric about a horizontal centreline in the diagram (i.e., the trace of the meridional plane). Similar to the colour convention used in Fig. 7, the colour map in Fig. 9 is selected such that a bluish patch represents a region of high (negative) value of  $\omega_S$  with fluid rotation in the clockwise direction and a reddish patch represents a region also of high  $\omega_S$  but with fluid rotation in the anti-clockwise direction (positive value).

The secondary flow field on plane G1P1 [station (a) in Fig. 9] consists of two similar counter-rotating vortices, one in each half of the cross section. Both are Dean vortices: the one in the top half is anti-clockwise while that in the bottom half is clockwise. The principle of distinguishing a Dean vortex from an anti-Dean vortex (when they occur together) based on the secondary fluid motion was explained in Fig. 7. Application of this principle establishes that the red patch (anti-clockwise) in the upper half of plane G2P1 in Fig. 9 [station (b)] represents the Dean vortex whereas the

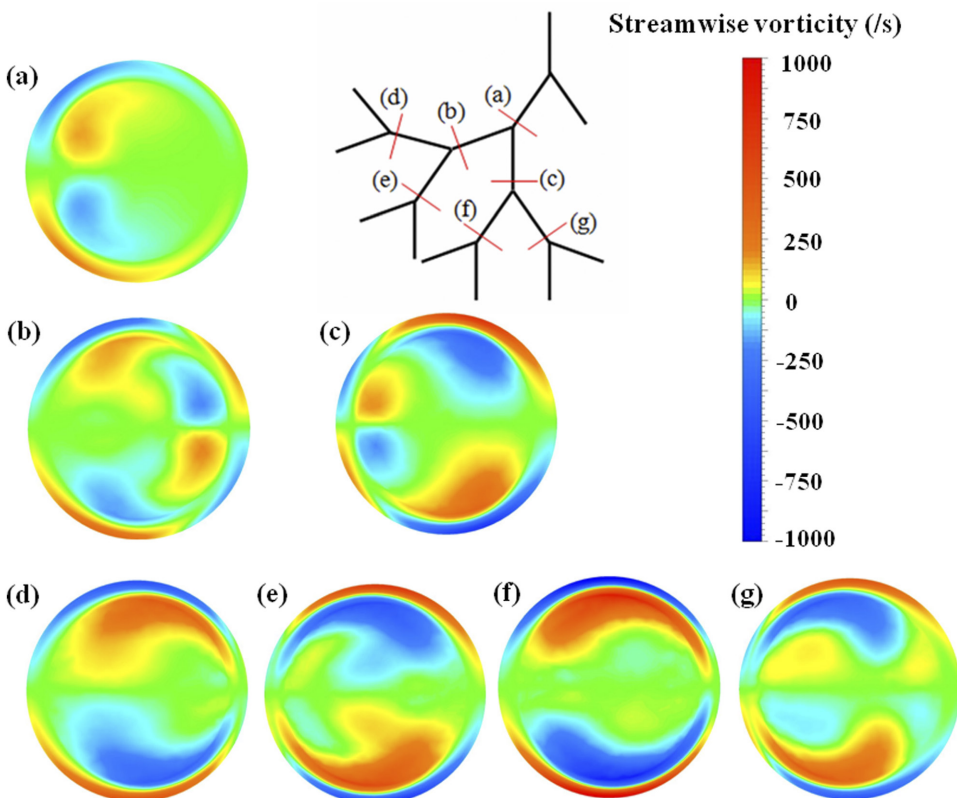


FIG. 9. Contours of streamwise vorticity  $\omega_S$  on the end-planes of branches of generations G1-G3 for  $Re = 1000$ ; in-plane configuration. (The representational convention is set such that the downstream bifurcation ridge appears as a vertical line in the diagram and the primary flow is towards the reader.)

blue patch (clockwise) in the same half of plane G2P1 represents the anti-Dean vortex. It must be noted that due to the opposite curvature of the flow path, the sense of rotation of the flow in the Dean vortices on plane G2P2 is opposite to that on plane G2P1. Therefore, the red patch (anti-clockwise) in the upper half of plane G2P2 in Fig. 9 [station (c)] represents the anti-Dean vortex whereas the blue patch (clockwise) in the same half of plane G2P2 represents the Dean vortex. The contours of  $\omega_S$  [at stations (d)-(g)] in Fig. 9 show that the two-vortex system, found in generation G1, is re-established on the end-planes of all branches of generation G3, instead of the four-vortex system found in all branches of generation G2.

A comparison of the contours of secondary velocity magnitude (Fig. 8) and streamwise vorticity parameters (Fig. 9) reveals that a region of small secondary velocity in the interior of a cross section maps to a region of high value of the streamwise vorticity parameter (this region usually corresponds to the vortex core). However, it is difficult to establish any further relations between the contours of  $|\vec{v}_S|$  and  $\omega_S$ . Hence, it is concluded that, although the pattern of the secondary velocity vectors is directly indicated by the contours of the streamwise vorticity parameter  $\omega_S$  (as demonstrated in Fig. 7), the contours of secondary velocity magnitude  $|\vec{v}_S|$  cannot easily be visualized from the contours of  $\omega_S$ . Consequently, we have included separate figures showing the contours of  $|\vec{v}_S|$  to present this complementary aspect of secondary motion.

In Figs. 8 and 9, the evolution of the secondary flow field was shown up to generation G3. Figure 10 shows a  $\lambda_2$  iso-surface in the in-plane configuration, depicting the vortices formed in the branches of generations G1-G4 of the G0-G5 network. Since regions with  $\lambda_2 < 0$  indicate the existence of a vortex, a particular negative value (normalized  $\lambda_2$  of  $-0.085$ ) is selected, by trial and error, that gives good flow visualization simultaneously for all four generations shown in the figure. The presence of four vortices in the flow field in the branches of generation G2 is clearly visible by the four strands of the  $\lambda_2$  iso-surface. The rather short lengths of the branches of generation G3 result in the lack of well-defined separate strands of  $\lambda_2$  iso-surfaces as found in the G2 branches. However, it was

found that the flow field in all G3 branches consists of two vortices (Fig. 9). The branches of generation G4 (except G4B8) are characterized by two well-defined strands depicting the presence of two vortices. The branch G4B8, to which the flow reaches after encountering one clockwise turn followed by three anti-clockwise turns, is characterized by four vortices (though the additional pair vanishes after a small distance in the branch). In the course of the present study, it was found that the flow fields in all the G5 branches show two vortices. Hence the flow field along the path G1B1-G5B15 (or G5B16) shows an alternation of two and four vortices (2 vortices in G1B1, 4 in G2B2, 2 in G3B4, 4 in G4B8, 2 in G5B15 or G5B16). Owing to the symmetry of the flow field in the in-plane configuration about the meridional plane, the vortices on any plane appear in pair (i.e., for each clockwise rotating vortex, there is an otherwise identical anticlockwise vortex). Another interesting observation that can be made in Fig. 10 is the persistence of the vortices up to longer distances in those G4 branches that are aligned with their grandmothers (this alignment brings in relatively more mass-flow in these branches<sup>1</sup>) as compared to the other G4 branches. Hence, it is inferred that, for the in-plane configuration, the persistence of the vortex structures in the branches of a generation broadly correlates with the mass-flow distribution pattern.

We have used all three parameters  $|\vec{v}_S|$ ,  $\omega_S$ , and  $\lambda_2$  for a comprehensive description of the secondary flow field because each has its own advantages as well as certain shortcomings. The  $\lambda_2$ -criterion is used to locate the core of vortices more precisely, it does not however provide any information on the sense of rotation of the flow in a vortex. The streamwise vorticity parameter  $\omega_S$  not only conveys the sense of rotation in a vortex through a change of sign but also captures the secondary boundary layer.  $\omega_S$  thus provides more physical insight into the description of the secondary motion in branched networks as compared to the  $\lambda_2$ -criterion. For either technique ( $\lambda_2$  or  $\omega_S$ ), the identification of fine details of the secondary flow field may be challenging if there are several vortices present. It is to be appreciated that the contours of  $\omega_S$  are indicative of the pattern of the secondary velocity vectors and not of the contours

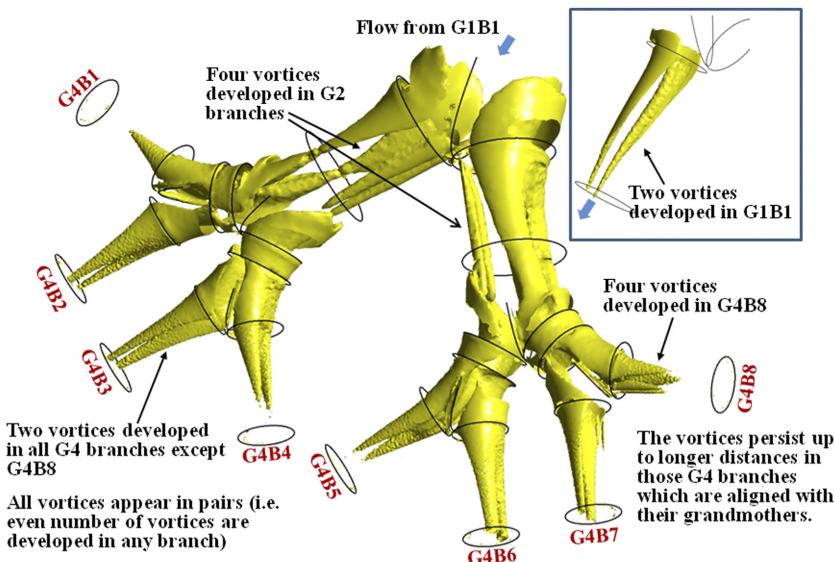


FIG. 10.  $\lambda_2$  iso-surface indicating three-dimensional evolution of the vortical structures in generations G1-G4 of a G0-G5 network at  $Re = 1000$ ; in-plane configuration.

of secondary velocity magnitude. Consequently, we have also included information about  $|\vec{v}_s|$  to present this complementary aspect of secondary motion.

Having built a comprehensive picture of the evolution of quantitative flow visualizations of secondary motion through three-dimensional branched networks, here, we formulate new parameters for a quantitative description of the overall features of the secondary flow field. These parameters are then used to assess the strength, non-uniformity, and evolution of secondary motion.

We first develop a measure for the strength of secondary motion. A new parameter  $E_{S/P}$  is defined as follows:

$$E_{S/P} = \sqrt{\frac{\int |\vec{v}_s|^2 |\vec{v}_p| dA}{\int |\vec{v}_p|^2 |\vec{v}_p| dA}}, \quad (12)$$

where  $dA$  is an elemental area on the cross-sectional plane and  $\vec{v}_s$  and  $\vec{v}_p$  are, respectively, the secondary and primary velocities. Equation (12) is formulated such that the parameter  $E_{S/P}$  represents the mass-flow-averaged relative kinetic energy of the secondary motion in an individual branch. The non-dimensionalization is performed with respect to the kinetic energy contained in the primary flow in the same branch. The quantity  $|\vec{v}_p|$  is used also in the numerator of the RHS of Eq. (12) because the mass-flow rate (throughflow) through a small elemental area  $dA$  is given by  $\rho |\vec{v}_p| dA$ . The condition  $E_{S/P} = 0$  indicates that there is no secondary motion in the cross-sectional plane of the particular branch. The condition

$E_{S/P} = 1$  signifies that on average the magnitude of secondary velocity in the plane is comparable to the magnitude of primary velocity.

It was shown previously (Figs. 4 and 5) that the maximum secondary velocity at a particular plane increases significantly as the inlet Reynolds number increases from 400 to 1000 (this trend is also seen to exist for computations performed up to  $Re = 1600$ ). However it is found that the value of  $E_{S/P}$  at a given location does not vary significantly with the variation of the inlet Reynolds number. We have therefore shown the evolution of  $E_{S/P}$  down the generations at one value of the inlet Reynolds number ( $Re = 1000$ ) in Fig. 11. It is observed that  $E_{S/P}$  decreases across the straight portion of a branch (i.e., from start-plane to end-plane). However, there occurs a considerable increase in  $E_{S/P}$  across a bifurcation module due to the introduction of fresh secondary motion on to the existing flow. As an example,  $E_{S/P}$  decreases from 0.299 at the start-plane of G1B1 to 0.078 on its end-plane; then it increases to 0.293 on the start-plane of G2B2, only to decrease to 0.076 at its end-plane. This contribution of the bifurcation modules in repeated enhancement of the secondary kinetic energy is responsible for the occurrence of significant values of  $E_{S/P}$  even in generation G5. (It should be remembered that  $E_{S/P}$  represents relative secondary kinetic energy, i.e., the secondary kinetic energy is normalized by the primary kinetic energy in the same branch.)

Figure 11 also shows that the increase in  $E_{S/P}$  across any bifurcation module, situated downstream of generation G1, is different along the two flow paths leading to its two daughter branches. For example, the value of  $E_{S/P}$  is found to increase

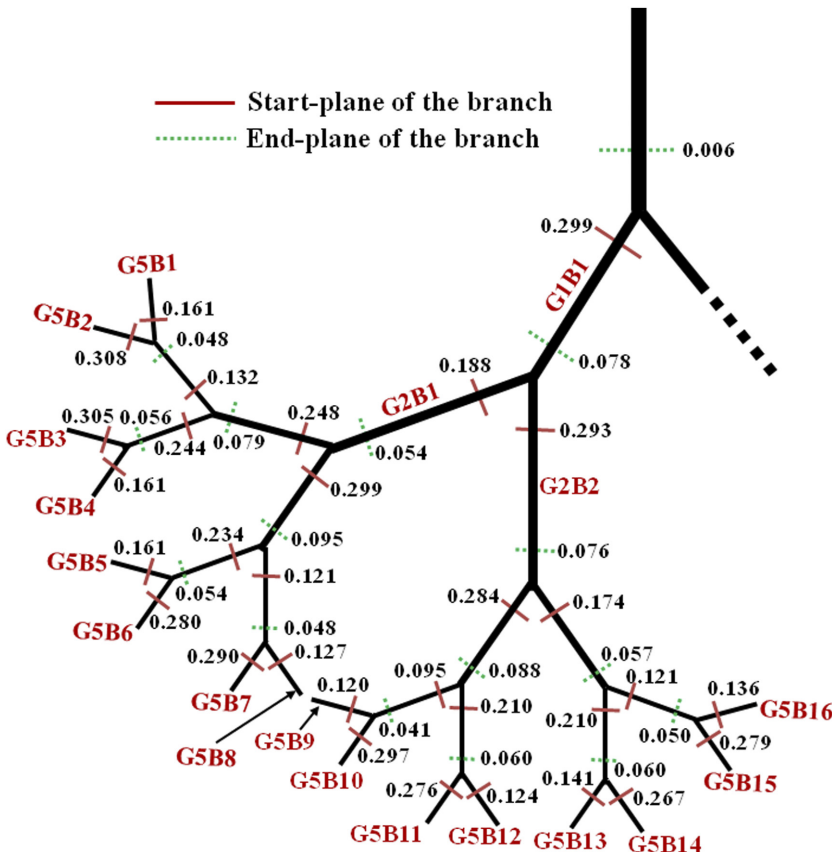


FIG. 11. Evolution of the relative secondary kinetic energy  $E_{S/P}$  down the generations in the G0-G5 network for  $Re = 1000$ ; in-plane configuration. (As a result of symmetry in the in-plane configuration, results are shown only for one-half of the entire network.)

from 0.078 at the end-plane of G1B1 to 0.188 at the start-plane of G2B1 and to 0.293 at the start-plane of G2B2. It was found in Ref. 1 that the mass-flow rate in G2B2 is greater than that in G2B1. Thus, the increase of  $E_{S/P}$  across a bifurcation module is greater along that path which has a greater mass-flow rate. This correlation is true for all the 30 bifurcation modules, situated downstream of generation G1, in the G0-G5 network. It is also observed in Fig. 11 that in a particular generation, the values of  $E_{S/P}$  are considerably larger in those branches which are aligned with their grandmother branches (these branches also have greater mass-flow rates by virtue of this alignment<sup>1</sup>), as compared to the others which are not aligned. For example, the value of  $E_{S/P}$  at the start plane of G2B2 (which is aligned with its grandmother G0B1) is considerably greater than that at the start-plane of G2B1. Out of the 16 branches of generation G5 shown in Fig. 11, eight (viz., B2, B3, B6, B7, B10, B11, B14, and B15) are parallel to their own grandmothers and the general levels of  $E_{S/P}$  in these branches are greater than that in the remaining eight branches. The alignment with the grandmother thus favours the generation of the secondary flow, but the mechanism is complex because of the non-uniform primary flow over the inlet cross-sectional area of a bifurcation module, flow division at the bifurcation ridge, and complex variations (in the flow direction) of the cross-sectional area and local curvature. As a result of this complexity, although the distribution of  $E_{S/P}$  is broadly in line with the mass-flow distribution (as observed above about the two cohorts of eight G5 branches each), an exact 1:1 mapping does not exist. For example, G5B11 and G5B1 have, respectively, the highest and lowest mass-flow rates, but G5B2 and G5B9 have, respectively, the highest and lowest values of  $E_{S/P}$  in generation G5.

While  $E_{S/P}$  gives a measure of the relative importance of the secondary motion at a particular cross-sectional plane, it does not give any direct indication of the non-uniformity in the secondary velocity field on that plane. Hence, we define a non-uniformity index  $\delta_{SF}$  for individual branches (at particular planes) as follows:

$$\delta_{SF} = \frac{\sqrt{\int (|\vec{v}_S| - \bar{v}_S)^2 dA}}{\sqrt{\pi R \bar{v}_S}}. \quad (13)$$

$\bar{v}_S$  is a measure of the average secondary velocity at that plane and is defined as follows:

$$\bar{v}_S = \sqrt{\frac{\int |\vec{v}_S|^2 dA}{\pi R^2}}. \quad (14)$$

Here,  $R$  is the radius of the branch in which the cross-sectional plane is located. One characteristic of this newly defined non-uniformity index  $\delta_{SF}$  is that for a uniform secondary flow field  $\delta_{SF} = 0$ . The greater, the value of  $\delta_{SF}$ , the greater is the non-uniformity of the secondary flow field at the chosen plane of the particular branch.

The values of  $\delta_{SF}$  at the start planes of the branches of generations G1-G5 are listed in Table IV for three values of the inlet Reynolds number. As a result of symmetry in in-plane configuration, results are shown only for one-half of the entire network. Even though the various contour plots of the

TABLE IV. Values of the non-uniformity index  $\delta_{SF}$  at the start-planes of the branches of generations G1-G5 for various inlet Reynolds numbers; in-plane configuration.

Branch	$Re = 400$	$Re = 1000$	$Re = 1600$
G1B1	0.489	0.443	0.423
G2B1	0.514	0.461	0.457
G2B2	0.552	0.483	0.446
G3B1	0.501	0.414	0.377
G3B2	0.514	0.429	0.432
G3B3	0.537	0.444	0.417
G3B4	0.509	0.447	0.437
G4B1	0.466	0.465	0.472
G4B2	0.581	0.508	0.467
G4B3	0.572	0.494	0.454
G4B4	0.477	0.485	0.509
G4B5	0.470	0.514	0.556
G4B6	0.594	0.548	0.518
G4B7	0.583	0.559	0.549
G4B8	0.489	0.520	0.506
G5B1	0.615	0.561	0.498
G5B2	0.661	0.584	0.532
G5B3	0.651	0.546	0.485
G5B4	0.601	0.511	0.490
G5B5	0.600	0.509	0.481
G5B6	0.638	0.573	0.538
G5B7	0.653	0.608	0.566
G5B8	0.603	0.545	0.534
G5B9	0.599	0.523	0.536
G5B10	0.650	0.605	0.569
G5B11	0.638	0.558	0.514
G5B12	0.565	0.536	0.593
G5B13	0.585	0.524	0.554
G5B14	0.644	0.576	0.534
G5B15	0.651	0.604	0.553
G5B16	0.607	0.545	0.554

secondary flow structure appear visually very different from one another (e.g., the secondary flow field in all branches of the G0-G5 network is characterized by a two-vortex system at  $Re = 400$ , whereas four-vortex systems develop in some branches at higher values of inlet Reynolds number), the values of  $\delta_{SF}$  are found to lie within a small range of 0.37 to 0.66. Up to generation G3, the values of  $\delta_{SF}$  are found to decrease as  $Re$  increases. In generation G4, the same trend (i.e., decrease of  $\delta_{SF}$  with increasing  $Re$ ) exists only in those branches which are aligned with their grandmothers. The same trend in the variation of  $\delta_{SF}$  with  $Re$  is found to hold true in most of the branches of generation G5 (except G5B9, G5B12, G5B13, and G5B16). For all three values of  $Re$  listed in Table IV, the maximum value of  $\delta_{SF}$  in generation G2 is found to be greater than that in generation G3; however, beyond G3, the maximum value of  $\delta_{SF}$  in a generation is found to increase as the flow travels down the generations.

## B. Analysis of secondary motion for out-of-plane configuration

The dimensions of the branches and the bifurcation angle in the out-of-plane configuration are identical to those of the in-plane configuration. However, the centrelines of all branches in the out-of-plane configuration do not lie on a single plane. The

planes containing the centrelines of branches of a generation are rotated through  $90^\circ$  with respect to the plane containing the centrelines of their mother and grandmother branches. The complexities associated with such a tortuous flow path in the out-of-plane configuration may be expected to give rise to flow fields that are considerably different from those observed for the in-plane configuration. It was shown in Ref. 1 that it is necessary and sufficient to determine the flow field in branches lying in one quarter of the network for the out-of-plane configuration. In the course of the present work, it is found that exactly the same conclusion holds true for the secondary flow field. Accordingly, here we present the secondary flow in a quarter of the network for the out-of-plane configuration.

### 1. General features of the secondary flow field

The flow paths in both the configurations are identical up to the end-planes of the branches of generation G1 (which is discussed in Sec. V A 1); hence, we begin here with a study of secondary motion in the next generation. In particular, we investigate the changes in the secondary flow across the straight portions of branches of generations G2 and G3 and that across the bifurcation modules connecting them. Figure 12 shows the secondary velocity vectors superposed on the contours of  $|\vec{v}_S|$  for  $Re = 400$ . Stations (a) and (b) correspond to the start-plane and end-plane of branch G2B1, stations (c) and (d) correspond to the start-plane and end-plane of branch G3B1, and stations (e) and (f) correspond to the start-plane and end-plane of branch G3B2. The representational convention is adopted such that the primary flow is towards the reader with the trace of the bifurcation ridge indicating its actual position and orientation with respect to the cross-sectional planes shown in the figure. An important feature of the secondary flow field in the out-of-plane configuration (Fig. 12) that distinguishes it from that in the in-plane configuration (Figs. 4 and 5) is the absence of any line of symmetry in the flow field at a cross section from generation G2 onwards.

Due to the representational convention adopted for Fig. 12, the direction of secondary motion on the cross-sectional planes in branch G2B1 [i.e., stations (a) and (b)] appear to be rotated through  $90^\circ$  with respect to the normal Dean-type flow. The secondary motion on these planes is governed by the curvature of the flow path in bifurcation module connecting branches G1B1, G2B1, and G2B2. For the  $90^\circ$  out-of-plane configuration, the bifurcation ridge shown in Fig. 12 is perpendicular to the above-mentioned bifurcation ridge (whose trace would thus appear as a horizontal line in the figure). This explains the rotation of the normal Dean-type flow through  $90^\circ$  at stations (a) and (b).

The change in the secondary flow field across the straight portion of a branch (from start-plane to end-plane) in generations G2 and G3 is demonstrated in Fig. 12. Similar to the observation made for the in-plane configuration, as the fluid travels along the straight portion of a branch in the out-of-plane configuration, the strength of the secondary flow is attenuated but the nature of the velocity field (i.e., number of vortices and sense of rotation in the vortices) is not

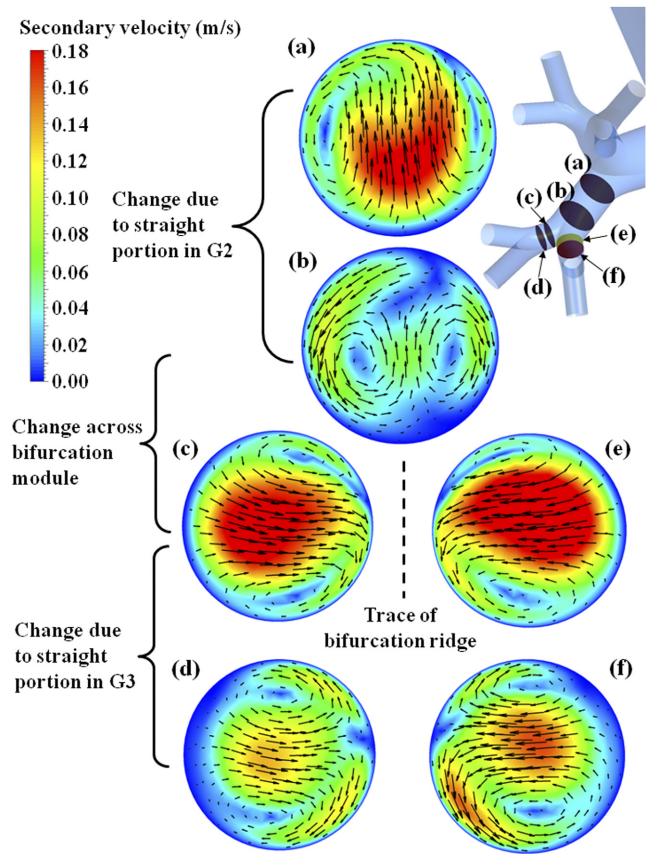


FIG. 12. Secondary velocity vectors superposed on the contours of secondary velocity magnitude on the start-planes and end-planes of branches G2B1, G3B1, and G3B2 for  $Re = 400$ ; out-of-plane configuration. (The length of the vectors on any cross-sectional plane indicates the secondary velocity scaled by the respective maximum secondary velocity on that plane.)

altered. There occurs a shift in the location of maximum secondary velocity from a central region towards the walls across the straight portion of the branch G2B1. However, due to the relatively short length of the branches of generation G3, the above-mentioned shift is only partial for the branches of generation G3.

Figure 12 also establishes the changes in the secondary flow pattern which occur across a bifurcation module. While station (b) corresponds to the start of the bifurcation module connecting G2B1, G3B1, and G3B2, stations (c) and (e) correspond to the end of the same module. Since the secondary motion on a cross-sectional plane is primarily governed by the curvature of flow path in the preceding bifurcation module, the direction of the secondary motion at stations (c) and (e) (which occurs downstream of the bifurcation ridge shown in Fig. 12) appears to be rotated through  $90^\circ$  with respect to that at station (b). The changes in the secondary flow that are observed to occur across the bifurcation module are as follows: (i) a significant increase in the maximum value of the secondary velocity, (ii) a shift of this maximum towards the central regions of the cross sections of the daughter branches, and (iii) a shift of the vortices towards the walls. The opposite sense of the secondary fluid motion observed on the start-plane of G3B2 [station (e)] as compared to that on the start-plane of G3B1 [station (c)] may be attributed to the opposite curvature along the two flow paths. A comparison of the contours of

secondary velocity magnitude at stations (c) and (e) shows that the maximum (and average) value of the secondary velocity is greater at station (e) than that at station (c). This is in line with the conclusion regarding mass-flow distribution in the branches of generation G3.<sup>1</sup>

Although the general features of the secondary flow shown in Fig. 12 hold good throughout the branching network for  $Re = 400$ , computations show that for  $Re \geq 1000$ , deviations from these general features occur at certain locations. A representative flow solution of this class is shown in Fig. 13 at  $Re = 1000$ . The stations (a)-(f) in Fig. 13 are the same as those in Fig. 12. The secondary flow field at stations (a) and (b) in Fig. 13 are characterized by three vortices as compared to the two-vortex system shown in Fig. 12, demonstrating the effect of the inlet Reynolds number on the vortical structure. (A comparison of the three vortices in Fig. 13 at  $Re = 1000$  with the four-vortex system developed at the same locations in the in-plane configuration of Fig. 5 for the same value of  $Re$  demonstrates the effects of the arrangement of the same individual branches on the vortical structure developed.) The secondary flow on the start-planes of G3B1 [station (c)] and G3B2 [station (e)] however show the usual two-vortex system similar to that found in a curved pipe.<sup>3</sup> This indicates that although the bifurcation module adds fresh secondary motion, the effects of local curvature dominate over the effects of upstream flow history.

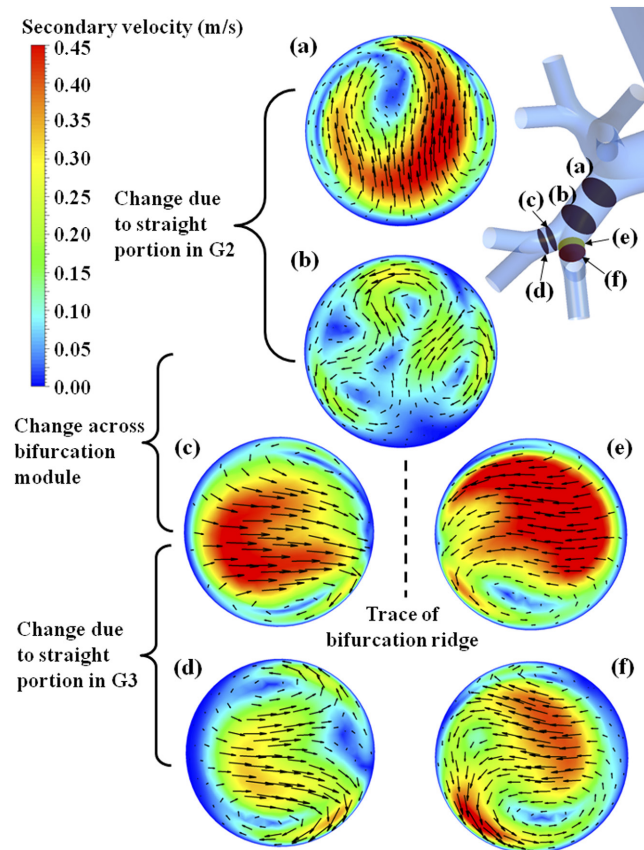


FIG. 13. Secondary velocity vectors superposed on the contours of secondary velocity magnitude on the start-planes and end-planes of branches G2B1, G3B1, and G3B2 for  $Re = 1000$ ; out-of-plane configuration. (The length of the vectors on any cross-sectional plane indicates the secondary velocity scaled by the respective maximum secondary velocity on that plane.)

The qualitative change of the secondary motion across the straight portion of a branch does not depend on the inlet Reynolds number. The general features consist of an attenuation of the secondary velocity in the flow direction, a shift of the location of maximum secondary velocity toward the periphery, and a shift of the centre of the vortices toward the centre of the cross section. As a result of the last feature, the three-vortex system becomes more clearly visible at the end-plane of the G2B1 [station (b) in Fig. 13], though the magnitude of the secondary velocity is considerably smaller there than at station (a).

Computations in the range  $400 \leq Re \leq 1600$  show that the magnitudes of the secondary velocity in the out-of-plane configuration increase significantly with the increase of the inlet Reynolds number. The absence of any line of symmetry in the secondary velocity field at a cross section from generation G2 onward in the out-of-plane configuration allows the occurrence of an odd number of vortices (three) in the branches of generation G2. A general observation that can be made from Figs. 12 and 13 is that the centres of the vortices are regions of low secondary velocity (as for the in-plane configuration). However, it is difficult to correlate the complete secondary flow structures with the contours of secondary velocity magnitude.

## 2. Three-dimensional modification of the secondary flow field in the complex internal passages of a bifurcation module

The bifurcation modules connecting the straight portions of branches of two successive generations in the out-of-plane configuration are structurally similar to those in the in-plane configuration. However, the three-dimensional arrangement of the branches in the  $90^\circ$  out-of-plane configuration is such that walls of the branch aligned with the inner and outer edges of the preceding bifurcation module get aligned with the top and bottom walls of the succeeding bifurcation module. As a consequence, the direction of action of the centrifugal force (from outer to inner edge of a bifurcation) at a cross section gets rotated through  $90^\circ$  after the flow crosses each bifurcation module.

Figure 14 shows how the internal passages of a bifurcation module modify the secondary velocity field. The bifurcation module connecting the branches G1B1, G2B1, and G2B2 is selected for the above purpose. In order to ensure that the planes in Fig. 14 capture the secondary motion properly, they must be constructed such that there is no component of primary motion along them. The method used to construct the planes in Fig. 6 is used in Fig. 14 as well. Station (a) corresponds to the end-plane of G1B1 (i.e., the start-plane of the bifurcation module). Station (c) corresponds to the cross-sectional plane passing through the point of intersection of the centrelines of G1B1, G2B1, and G2B2 and with normal along the centreline of G1B1. Station (b) is located midway between stations (a) and (c). Stations (e) and (f) correspond to the start-planes of G2B1 and G2B2, respectively. The bifurcation angle for this configuration is the same as that for the in-plane configuration ( $70^\circ$ ). Hence, as in Fig. 6, station (d) in Fig. 14 is defined at that location where the flow path has been diverted through  $17.5^\circ$  with respect to the centreline of G1B1. The

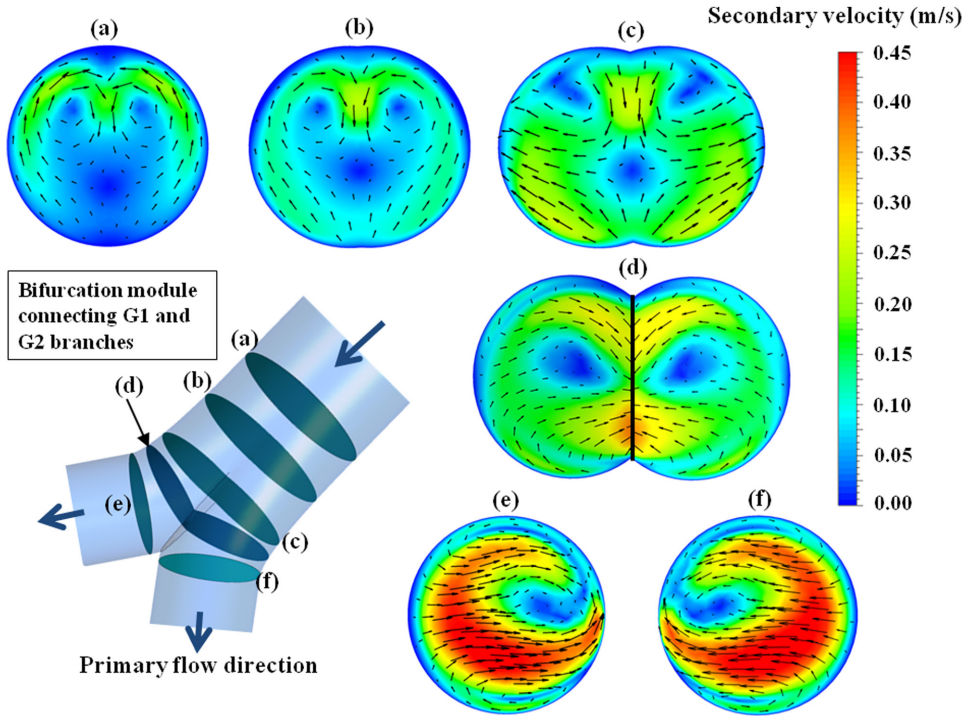


FIG. 14. Changes in the secondary flow field across the bifurcation module connecting G1B1, G2B1 and G2B2 branches for  $Re = 1000$ ; out-of-plane configuration. (The representational convention is selected such that the trace of the bifurcation ridge appears as a vertical line in the diagram and the primary flow is towards the reader.)

cross section at station (d) consists of two planes subtending an angle of  $145^\circ$  on the upstream side, intersecting along a line which coincides with the trace of the bifurcation ridge at station (d).

The fluid traverses only one bifurcation module (that joining G0 and G1 branches) before arriving at the inlet plane of the module shown in Fig. 14. Hence the secondary velocity field at station (a) is qualitatively similar to the Dean type flow observed in a curved pipe. The representational convention is adopted such that the trace of the bifurcation ridge (of the module shown in Fig. 14) appears as a vertical line in the diagram. Owing to the orthogonality of two successive flow units, the trace of the preceding bifurcation ridge would appear as a horizontal line. This results in the rotation of the normal Dean type flow pattern through  $90^\circ$  at stations (a) and (b). At station (c), there occurs a distinct secondary motion of fluid towards the outer edges of the bifurcation. This motion of the fluid may be attributed to the combined effects of the presence of the downstream bifurcation ridge and the gradual flattening of the cross section in the bifurcation module between stations (b) and (c). Similar to the observation made in Fig. 6 for the in-plane configuration, Fig. 14 shows that there occurs a reversal of the secondary motion (i.e., from the outer edges of the bifurcation towards the centre of the cross section) at station (d) due to the dominance of local curvature effects. The secondary motion at stations (e) and (f) is characterized by considerably greater velocities as compared to that at station (d) and the presence of three vortices, two of which appear near the top and bottom walls and one appears near the inner edge of the bifurcation.

A comparison of the magnitudes of the secondary velocity  $|\vec{v}_S|$  at the inlet plane [station (a)] with that at the outlet planes [stations (e) and (f)] shows that the bifurcation module significantly increases the secondary velocity magnitudes. At station (a) in Fig. 14, the secondary motion drives fluid

from the top wall towards the bottom wall along the central region of the cross section, and back along the left and right walls towards the top wall. At stations (e) and (f), the vectors show that the secondary motion is directed from the outer edges to the inner edge of the bifurcation along the central regions, and back along the top and bottom walls towards the outer edges of the bifurcation. Thus the bifurcation module in the out-of-plane configuration changes the direction of the secondary motion, causing a  $90^\circ$  rotation of the secondary flow structures. Moreover, the selected bifurcation module alters the number of vortices; a two-vortex system at station (a) is converted to a three-vortex system at stations (e) and (f). However, the same bifurcation module preserves certain symmetry present at its inlet plane. The symmetry of the secondary flow about the vertical line is preserved, leading to the development of identical (mirror images) secondary flow structures in the two daughter branches [stations (e) and (f)].

### 3. Evolution of secondary flow for out-of-plane configuration

Having discussed the general features of the secondary flow in the branching network, we now focus on the spatial evolution of the secondary flow as the fluid travels down the generations from G0 to G5. We build a comprehensive picture of the evolution of secondary motion through contours of  $|\vec{v}_S|$ ,  $\omega_S$ , and  $\lambda_2$ . In addition to this, the new parameters (viz.,  $E_{S/P}$ ,  $\delta_{SF}$ , and  $\delta_{Gn}$ ) are used to give a quantitative description of the overall features of the secondary flow field. As mentioned previously, the secondary flow field in the out-of-plane configuration is such that it is necessary and sufficient to determine the flow field in a quarter of the network. Accordingly, here we present the secondary flow details in the branches in one quarter of the network (i.e., in the branches originating from G2B1).

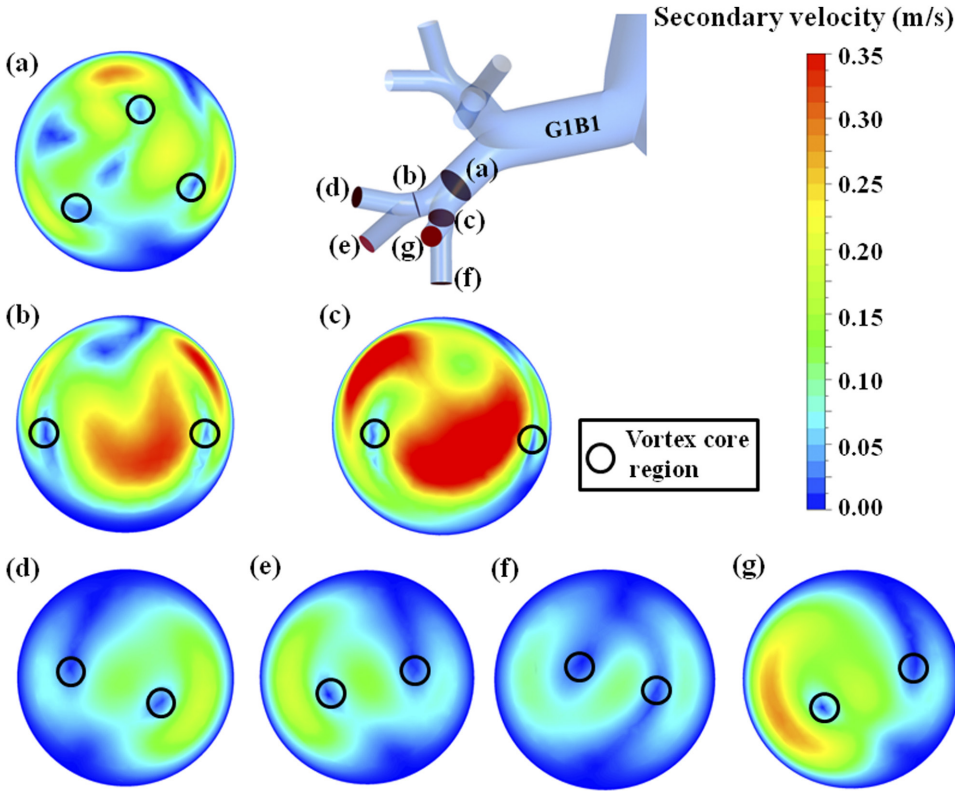


FIG. 15. Contours of secondary velocity magnitude at the end-planes of branches of generations G2-G4 for  $Re = 1000$ ; out-of-plane configuration. (The representational convention is set such that the downstream bifurcation ridge appears as a vertical line in the diagram and the primary flow is towards the reader.)

Figure 15 shows the contours of the secondary velocity magnitude  $|\vec{v}_S|$  on the end-planes of the branches of generations G2 to G4 for the out-of-plane configuration at  $Re = 1000$ . The stations [(a)-(g)] at which the contour plots are presented are shown in the schematic diagram within Fig. 15. The contour of  $|\vec{v}_S|$  on the end-plane of G1B1 for this configuration is similar to that at the same location in the in-plane configuration [station (a) in Fig. 8] owing to identical flow paths up to that location for both configurations. Hence, in Fig. 15, we begin with the contour of  $|\vec{v}_S|$  on the end-plane of G2B1. It is observed that there exists no line of symmetry for the secondary velocity field on the end-planes of branches of generations G2-G4 in the out-of-plane configuration.

The  $\lambda_2$ -criterion<sup>36</sup> has been used for locating the cores of the vortices (denoted by small circles in Fig. 15) where the secondary velocity is usually low. Contrary to the existence of two pairs of vortices in the in-plane configuration, the end-planes of the branches of generation G2 in the out-of-plane configuration are marked by three vortices. The secondary flow patterns on the end-planes of the branches of generations G3 and G4 are again characterized by two dissimilar vortices (due to lack of any line of symmetry). The vortices in the cross section are shifted from their expected positions (near the top and bottom walls) as observed in curved pipes or at the end-planes of G3 branches in the in-plane configuration (Fig. 8). This apparent shift in the location of the vortices is due to the combined effects of the rotation of successive flow units through  $90^\circ$  in this configuration and the adopted representational convention.

Having discussed the nature of vortical structures, we now turn our attention to the magnitudes of secondary velocity. Figure 15 shows that the maximum (and average) secondary

velocity on plane of G3P2 is greater than that on G3P1. It was established in Ref. 1 that the mass-flow rate in branch G3B2 is greater than that in branch G3B1. Moreover, among the G4 branches, G4B4 [station (g)] shows the greatest value of the maximum (and average) secondary velocity; the same branch was found to have the greatest mass-flow rate.<sup>1</sup> Thus, it is established here that the secondary velocity is greater at the end-plane of that branch which has a higher mass-flow rate.

It has been established in Figs. 12 and 13 that the maximum secondary velocity generally occurs at central locations on the cross section at the start of the straight portion of a branch, and that it has the general tendency to shift towards the walls as the flow progresses to the end plane of that branch. This shifting is complete on the end-planes of branches of generations G2 and G4, while the shift is partial on the end-planes of the branches of G3 [stations (b) and (c)], as shown in Fig. 15, for short lengths of the branches of this generation.

The correlation between the patterns of secondary velocity vectors and streamwise vorticity  $\omega_S$  on a cross-sectional plane that was established in Fig. 7 for the in-plane configuration is found to hold good for the out-of-plane configuration as well. Figure 16 shows the spatial evolution of  $\omega_S$  in the branched network for  $Re = 1000$ . The schematic diagram within the figure shows the locations of the cross-sectional planes in generations G2-G4 [stations (a)-(g)] on which the contours of  $\omega_S$  are plotted. Similar to the colour convention used in Figs. 7 and 9, the colour map in Fig. 16 is selected such that a bluish patch represents a region of high (negative) value of  $\omega_S$  with fluid rotation in the clockwise direction and a reddish patch represents a region also of high  $\omega_S$  but

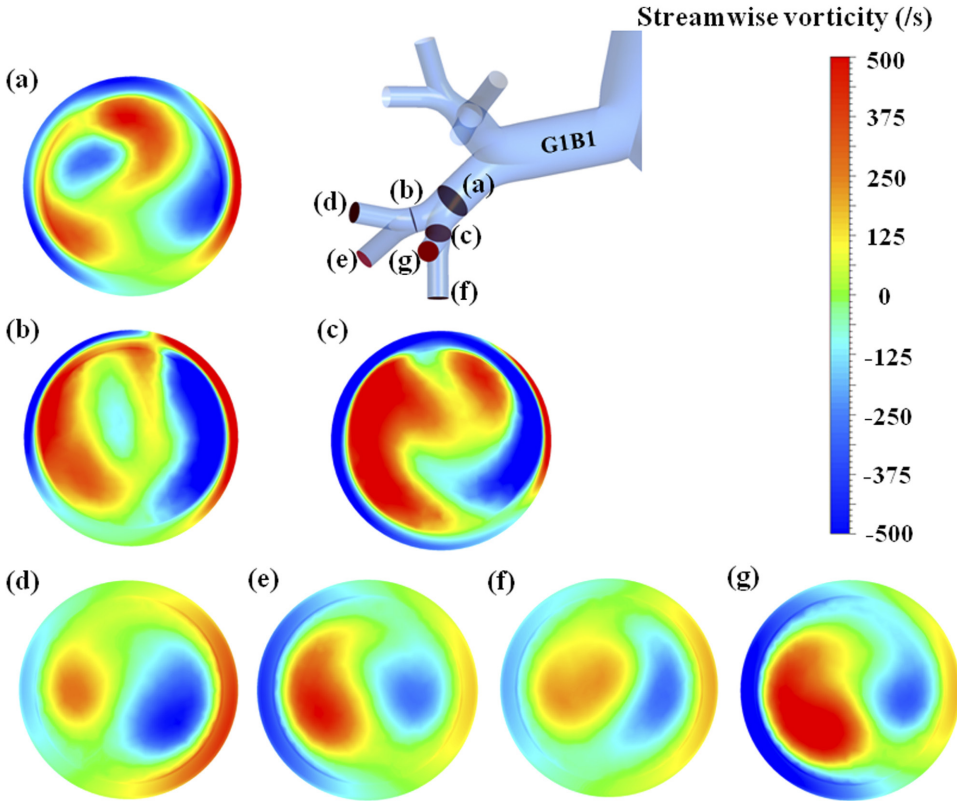


FIG. 16. Contours of streamwise vorticity  $\omega_S$  at the end-planes of branches of generations G2-G4 for  $Re = 1000$ ; out-of-plane configuration. (The representational convention is set such that the downstream bifurcation ridge appears as a vertical line in the diagram and the primary flow is towards the reader.)

with fluid rotation in the anti-clockwise direction (positive value).

The contours of  $\omega_S$  at station (a) in Fig. 16 shows three vortices (two anti-clockwise vortices indicated by the red patches and one clockwise vortex indicated by the blue patch on the right) that were denoted by small circles in Fig. 15. The contours of  $\omega_S$  on the end-planes of the branches of generations G3 [stations (b) and (c)] and G4 [stations (d)-(g)] in Fig. 16 show that the two-vortex system is re-established. The apparent change in the position of these vortices (the vortices appear near the left and right walls instead of the top and bottom walls) is due to the combined effects of the three-dimensional arrangement of the branches in this configuration and the adopted representational convention, as explained in the context of Fig. 15. It must be noted that while the two vortices occurring in a pair at any cross section in the in-plane configuration are similar and counter-rotating, those occurring in pairs in a branch downstream of generation G1 in the out-of-plane configuration, are counter-rotating but dissimilar.

A comparison of the contours of secondary velocity magnitude (Fig. 15) and the streamwise vorticity parameter (Fig. 16) reveals that a region of small secondary velocity in the interior of a cross section maps to a region of high value of a the streamwise vorticity parameter (this region usually corresponds to the vortex core). However, it is difficult to establish any further relations between the contours of  $|\vec{v}_S|$  and  $\omega_S$ .

Figure 17 shows a  $\lambda_2$  iso-surface in the out-of-plane configuration, depicting the vortices formed in the branches of generations G1 to G4 of a G0-G5 network (owing to the established symmetry in the flow field, only a quarter of the network

is shown here). Since regions with  $\lambda_2 < 0$  indicate the existence of a vortex, a particular negative value (normalized  $\lambda_2$  of  $-0.07$ ) is selected, by trial and error, that gives good flow visualization simultaneously for all four generations shown in the figure. The presence of three vortices in the flow field in the branch G2B1 is clearly visible by the three separate strands of the  $\lambda_2$  iso-surface. Each branch of generation G3 has two separate strands of  $\lambda_2$  iso-surfaces but the strands are not as well-defined as they are in generation G2; this is due to rather short lengths of the branches of generation G3. It was seen in Fig. 10 (for in-plane configuration) that all vortices in the G4 branches occur in pairs, and the two vortices forming a pair are similar to each other. This similarity is due to the symmetry of the flow field about the meridional plane of the in-plane configuration. However, in the out-of-plane configuration (Fig. 17), the flow field in the branches originating from any one of the four G2 branches are all different from one another and do not possess any plane of symmetry. Consequently, the order found in the vortex structure for in-plane configuration is absent here; there are twelve branches of generation G4 for the out-of-plane configuration which contain two dissimilar vortices each, and there are four branches (e.g., G4B3) which contain an odd number (three) of vortices (i.e., the vortices are not even paired in these branches). An interesting observation is that, if one follows the path from G1B1 to G5B5 (or G5B6) at high inlet Reynolds number (e.g.,  $Re = 1000$  or  $Re = 1600$ ), one would encounter an alternation of two-vortex and three-vortex systems (2 vortices in G1B1, 3 in G2B1, 2 in G3B2, 3 in G4B3, 2 in G5B5 or G5B6).

It was seen in Fig. 10 that the vortices persisted up to longer distances in the G4 branches of the in-plane configuration, which are aligned with their grandmothers. However,

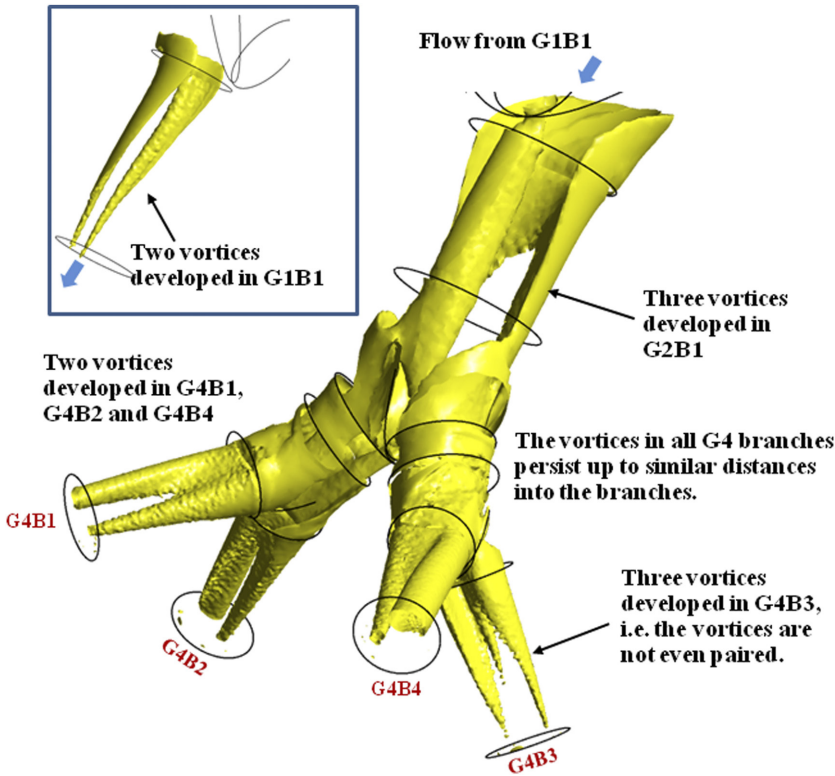


FIG. 17.  $\lambda_2$  iso-surface indicating three-dimensional evolution of the vortical structures in generations G1-G4 of a G0-G5 network at  $Re = 1000$ ; out-of-plane configuration.

Fig. 17 shows that the vortices in all G4 branches (barring one of the three vortices in G4B3 and its homologues) persist up to similar distances into the branch for the out-of-plane configuration. This behaviour may be attributed to the smaller degree of non-uniformity in the mass-flow distribution in this configuration.<sup>1</sup> The fact that one of the three vortices in G4B3 shown in Fig. 17 does not persist up to the end-plane of G4B3 is reflected in the appearance of only two vortices in the contours of  $\omega_S$  constructed on the end-plane of G4B3 shown previously in Figs. 15(f) and 16(f).

The strength of the secondary flow for the out-of-plane configuration is also quantified by the relative secondary kinetic energy  $E_{S/P}$  defined in Eq. (12). It is shown in Figs. 12 and 13 that the maximum secondary velocity at a particular plane increases significantly as the inlet Reynolds number increases from 400 to 1000 (this trend is also seen to exist for computations performed up to  $Re = 1600$ ). However, similar to the in-plane configuration, the values of  $E_{S/P}$  for the out-of-plane configuration also do not vary significantly with the variation of  $Re$ . We therefore show the evolution of  $E_{S/P}$  down the generations of the out-of-plane configuration at  $Re = 1000$  only (Fig. 18). The value of  $E_{S/P}$  is found to decrease appreciably across the straight portion of a branch (i.e., from start-plane to end-plane of the branch). However, there occurs a considerable increase in the secondary flow strength across a bifurcation module due to the introduction of fresh secondary motion to the existing flow. This contribution of the bifurcation modules in repeated enhancement of the secondary kinetic energy is responsible for the occurrence of significant values of  $E_{S/P}$  even in generation G5. A comparison of Figs. 11 and 18 shows that the levels of  $E_{S/P}$  are greater in the out-of-plane than in the in-plane configurations. This may be attributed to the more tortuous flow path in the out-of-plane

configuration resulting in the generation of greater secondary motion.

Table V shows the values of the non-uniformity index  $\delta_{SF}$  [defined in Eq. (13)] at the start-planes of the branches of generations G1-G5 for three values of the inlet Reynolds

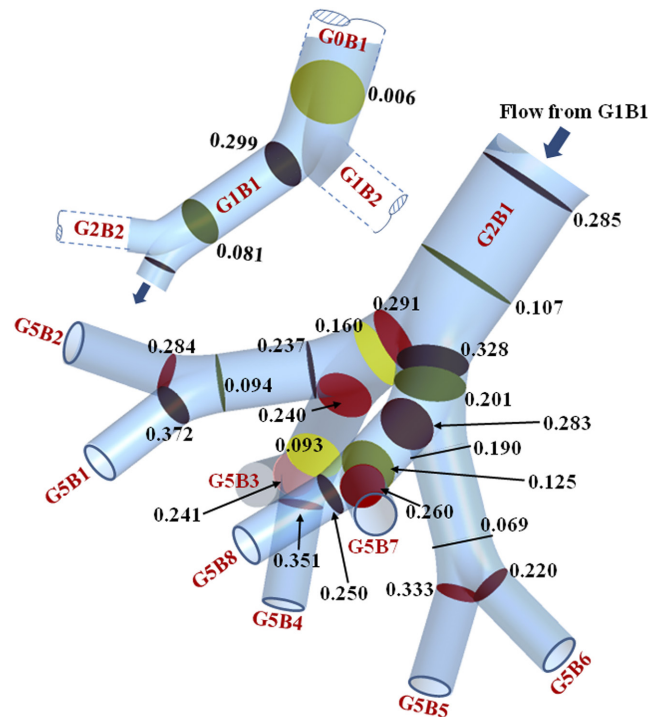


FIG. 18. Evolution of the relative secondary kinetic energy  $E_{S/P}$  down the generations in the G0-G5 network for  $Re = 1000$ ; out-of-plane configuration. (As a result of symmetry in out-of-plane configuration, results are shown only for one-fourth of the entire network.)

TABLE V. Values of the non-uniformity index  $\delta_{SF}$  at the start-planes of the branches of generations G1-G5 for various inlet Reynolds numbers; out-of-plane configuration.

Branch	$Re = 400$	$Re = 1000$	$Re = 1600$
G1B1	0.489	0.443	0.425
G2B1	0.521	0.452	0.441
G3B1	0.528	0.467	0.440
G3B2	0.538	0.468	0.445
G4B1	0.573	0.518	0.503
G4B2	0.546	0.530	0.511
G4B3	0.539	0.502	0.567
G4B4	0.581	0.551	0.530
G5B1	0.623	0.593	0.595
G5B2	0.607	0.559	0.598
G5B3	0.608	0.553	0.607
G5B4	0.623	0.579	0.539
G5B5	0.620	0.582	0.572
G5B6	0.596	0.525	0.524
G5B7	0.599	0.626	0.623
G5B8	0.619	0.602	0.621

number. As a result of symmetry explained at the beginning of Sec. V B dedicated to the out-of-plane configuration, Table V shows results only for one-fourth of the entire network. As in the case of the in-plane configuration (Table IV), the values of  $\delta_{SF}$  in Table V are found to lie within a small range of 0.43 to 0.62. For branches of generations G1, G2, and G3,  $\delta_{SF}$  is found to decrease as the inlet Reynolds number increases from 400 to 1600. In generation G4, the same trend (i.e., decrease of  $\delta_{SF}$  with increasing  $Re$ ) exists for all branches except G4B3 (and its homologues). However, it is difficult to establish any definite trend in the variation of  $\delta_{SF}$  with  $Re$  in the branches of generation G5. For all three values of  $Re$  listed in Table V, the maximum value of  $\delta_{SF}$  in a generation increases monotonically from G1 to G5. Another interesting characteristic of  $\delta_{SF}$  in the out-of-plane configuration is that for a given inlet Reynolds number, the variation of  $\delta_{SF}$  in a particular generation is appreciably smaller than the same in the in-plane configuration.

### C. Non-uniformity of secondary motion in a generation and its downstream evolution

Both  $E_{S/P}$  defined by Eq. (12) and  $\delta_{SF}$  defined by Eq. (13) are parameters that quantify the overall characteristics of secondary flow on a cross-sectional plane of a particular branch. A further overall parameter  $\delta_{Gn}$  is defined below to quantify the degree of non-uniformity in secondary motion among the branches of a particular generation  $Gn$ ,

$$\delta_{Gn} = (\bar{v}_{S,Gn,max} - \bar{v}_{S,Gn,min}) / \bar{v}_{S,Gn,avg}. \quad (15)$$

$\bar{v}_S$  values are calculated by Eq. (14) at homologous locations in all the branches of a particular generation  $Gn$ : the maximum of this cohort is designated by  $\bar{v}_{S,Gn,max}$ , the minimum of this cohort is designated by  $\bar{v}_{S,Gn,min}$ , and  $\bar{v}_{S,Gn,avg}$  is the arithmetic mean of the  $\bar{v}_S$  values in all branches belonging to the generation  $Gn$ . The condition  $\delta_{Gn} = 0$  indicates that all branches of the chosen generation have the same value for  $\bar{v}_S$ . The greater

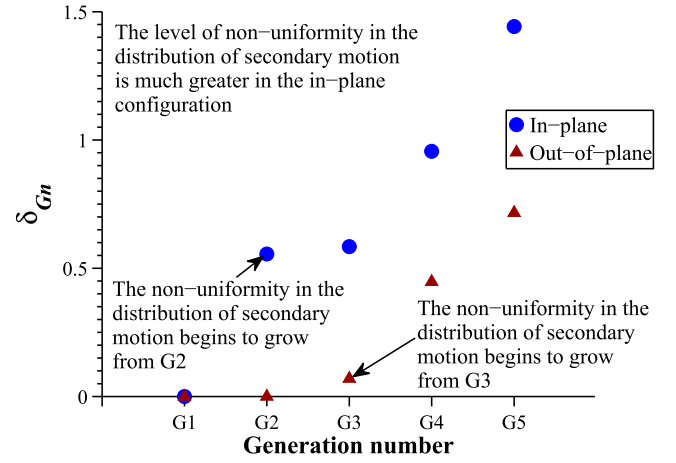


FIG. 19. Evolution of  $\delta_{Gn}$  with increasing generation number for both in-plane and out-of-plane configurations at  $Re = 1000$ .

the value of  $\delta_{Gn}$ , the greater is the non-uniformity in the distribution of secondary flow among the branches of generation  $Gn$ .

Figure 19 shows that  $\delta_{Gn}$  grows as the generation number  $Gn$  increases. For a given inlet Reynolds number, the value of  $\delta_{Gn}$  in a particular generation in the out-of-plane configuration is appreciably smaller than the same in the in-plane configuration. This is in line with the conclusion regarding mass-flow distribution in various branches of a generation.<sup>1</sup>

## VI. CONCLUSION

A major aim of the present work is to understand and thoroughly document the generation, the three-dimensional distribution, and the evolution of secondary motion as the fluid progresses downstream through a branched network. Six generations of branches (involving 63 straight portions and 31 bifurcation modules) are computed in one go; such computational challenges are rarely taken in the literature. Since accurate capturing of the fine details of secondary motion is more challenging than capturing the primary flow field, we recomputed the entire flow field through the same three-dimensional geometry of flow passages given in Ref. 1 using a much finer mesh here; more than  $30 \times 10^6$  computational elements are used. Results are presented for three values of inlet Reynolds number: 400, 1000, and 1600, and two different three-dimensional arrangements of the same individual branches—in-plane and out-of-plane.

As compared to the secondary motion in a simple curved pipe,<sup>3</sup> three distinctive features, viz., the change of shape and size of flow-cross-section, the division of non-uniform primary flow in a bifurcation module, and repeated switchover from clockwise to anticlockwise curvature and vice versa in the flow path, make the present situation more complex. Another complexity arises due to the consideration of two three-dimensional branching configurations, in-plane and out-of-plane, side by side. It is shown that the straight portions in the network, in general, attenuate secondary motion, while the three-dimensionally complex bifurcation modules generate and alter the nature of secondary motion (Figs. 4–6, 10–14, 17, and 18). Across a bifurcation module, the locations of

maximum secondary velocity tend to shift toward the central regions of the cross sections of the daughter branches and the centres of vortices tend to shift toward the walls. Along the straight portions, on the other hand, the locations of the maximum secondary velocity tend to move toward the walls, whereas the centres of vortices tend to move toward the centre of the cross section.

On the basis of the primary flow field, an important conclusion was reached in Ref. 1 that in the in-plane configuration, for every branch there is one (and only one) other branch in the same generation (from G2 onward) where the flow field is identical, and for the out-of-plane configuration, for every branch there are three (and exactly three) other branches in the same generation (from G3 onward) where the flow fields are identical. It is established in the present work that the same conclusion holds true also regarding the secondary velocity field. For example, for the in-plane configuration, the secondary flow field in branch G5B1 is identical to that in branch G5B32 (and the secondary flow field in all other branches of G5 is different from that in G5B1 and G5B32), and for out-of-plane configuration, the secondary flow field in branch G5B1 is identical to that in branches G5B16, G5B17, and G5B32. Another feature about the symmetry of flow field on a cross-sectional plane in any particular branch, established in connection with primary flow in Ref. 1, also holds true for the secondary flow. It is found that, for the in-plane configuration, the secondary flow field is symmetric about the meridional plane in all branches, but for the out-of-plane configuration there exists no line of symmetry on a cross-sectional plane in any branch from generation G2 onward. It was shown in Ref. 1 that the modular approach or the truncation approach, often used in the literature to drastically reduce the number of branches in a generation for which CFD solutions are obtained, have serious limitations in accurately determining the primary flow field. The modular or truncation approach has similar limitations in determining the secondary flow field.

We have used all three parameters,  $|\vec{v}_S|$ ,  $\omega_S$ , and  $\lambda_2$ , for a comprehensive description of the secondary flow field because each has its own advantages as well as certain shortcomings. The  $\lambda_2$ -criterion is used to locate the core of vortices more precisely; it does not however provide any information on the sense of rotation of the flow in a vortex. The streamwise vorticity parameter  $\omega_S$  not only conveys the sense of rotation in a vortex through a change of sign but also captures the secondary boundary layer (Fig. 7).  $\omega_S$  thus provides more physical insight into the description of the secondary motion in branched networks as compared to the  $\lambda_2$ -criterion. It is to be appreciated that the contours of streamwise vorticity are indicative of the pattern of the secondary velocity vectors and not of the contours of secondary velocity magnitude. Thus contours of  $|\vec{v}_S|$  are constructed in Figs. 4–6, 8, and 12–15 to present this complementary aspect of the secondary motion.

The three-dimensional modification of the secondary flow field in a single bifurcation module is similar in both configurations (Figs. 6 and 14), and is primarily governed by the local curvature of the flow path in the module. The number, arrangement, and structure of vortices may be altered as the flow passes through a bifurcation module (e.g., Fig. 10 shows

how a bifurcation module modifies a two-vortex system in G1B1 into a four-vortex system in G2B1 or G2B2). A bifurcation module, on the other hand, preserves certain symmetry present at its inlet plane: if the line of symmetry at inlet is along the bifurcation ridge, then the secondary flow structure in the daughter branches would be identical, and if the line of symmetry at inlet lies on the meridional plane, then for each daughter branch the secondary flow in the two halves of the individual cross sections would be identical. However, the rotation of successive flow units through  $90^\circ$  in the out-of-plane configuration results in the gradual distortion of the secondary flow field down the generations leading to a lack of any order in the flow field (considering only one quarter of the network). Thus, whereas for the in-plane configuration the vortices on any plane appear in pair (i.e., for each clockwise rotating vortex there is an otherwise identical anticlockwise vortex), the vortices on a plane for out-of-plane configuration may be dissimilar and there may be odd number of vortices [e.g., three vortices in G2B1 shown in Fig. 15(a) or three in G4B3 shown in Fig. 17]. Second, whereas the vortices in the in-plane configuration can be described as the usual Dean or anti-Dean vortices, the shapes and orientations of the vortices in the out-of-plane configuration may be such that they do not conform to the conventional Dean or anti-Dean type.

The details of the secondary flow field and the vortical structures in a branched network are analysed comprehensively and many subtle features are unearthed. As an example, it is shown that at low inlet Reynolds number (e.g.,  $Re = 400$ ) all branches in generation G1 onward exhibit a two-vortex system whereas 2, 3, or 4 vortices may occur at higher inlet Reynolds number. If one follows the path from G1B1 to G5B15 (or G5B16) in the in-plane configuration at high inlet Reynolds number (e.g.,  $Re = 1000$  or  $Re = 1600$ ), one would encounter an alternation of two-vortex and four-vortex systems (2 vortices in G1B1, 4 in G2B2, 2 in G3B4, 4 in G4B8, 2 in G5B15 or G5B16). Similarly, in the out-of-plane configuration, if one follows the path from G1B1 to G5B5 (or G5B6) at high inlet Reynolds number (e.g.,  $Re = 1000$  or  $Re = 1600$ ), one would encounter an alternation of two-vortex and three-vortex systems. For both configurations, the persistence of the vortex structures in the branches of a generation broadly correlates with the mass-flow distribution pattern.

Other than providing a comprehensive picture of the evolution of quantitative flow visualizations of secondary motion through three-dimensional branched networks (e.g., contours of  $|\vec{v}_S|$ ,  $\omega_S$ , and  $\lambda_2$ ), we have formulated three new parameters ( $E_{S/P}$ ,  $\delta_{SF}$ , and  $\delta_{Gn}$ ) for a quantitative description of the overall features of the secondary flow field.  $\delta_{SF}$  represents a non-uniformity index of the secondary flow in an individual branch,  $E_{S/P}$  represents the mass-flow-averaged relative kinetic energy of secondary motion in an individual branch, and  $\delta_{Gn}$  provides a measure of the non-uniformity of secondary flow between various branches of the same generation  $Gn$ .

The repeated enhancement of the secondary kinetic energy in the bifurcation modules is responsible for the occurrence of significant values of  $E_{S/P}$  even in generation G5 (Figs. 11 and 18). For the in-plane configuration, the alignment of any branch with its own grandmother favours the generation of secondary flow. For both configurations, it is found that for

any bifurcation module, the value of  $E_{S/P}$  is greater in that daughter branch in which the mass-flow rate is greater. In general, the levels of  $E_{S/P}$  are greater in the out-of-plane than in the in-plane configuration. This may be attributed to the more tortuous flow path in the out-of-plane configuration resulting in the generation of greater secondary motion.

Even though the various contour plots of the complex secondary flow structure appear visually very different from one another, the values of  $\delta_{SF}$  are found to lie within a small range ( $0.37 \leq \delta_{SF} \leq 0.66$ ) for the six-generation networks studied. For the out-of-plane configuration, the maximum value of  $\delta_{SF}$  in a generation increases monotonically from G1 to G5 (Table V). For the in-plane configuration, this monotonicity is maintained from generation G3 onward (Table IV).

Figure 19 shows that  $\delta_{Gn}$  grows as the generation number  $Gn$  increases. For a given inlet Reynolds number, the value of  $\delta_{Gn}$  in a particular generation in the out-of-plane configuration is appreciably smaller than the same in the in-plane configuration (this is in line with the conclusion regarding mass-flow distribution in various branches of a generation<sup>1</sup>). Thus it is found that the out-of-plane configuration, in general, creates more secondary kinetic energy (higher  $E_{S/P}$ ), similar level of non-uniformity in secondary flow in an individual branch (similar  $\delta_{SF}$ ), and significantly lower level of non-uniformity in the distribution of secondary motion among various branches of the same generation (much lower  $\delta_{Gn}$ ), as compared to the in-plane arrangement of the same branches.

<sup>1</sup>A. Guha, K. Pradhan, and P. K. Halder, "Finding order in complexity: A study of the fluid dynamics in a three-dimensional branching network," *Phys. Fluids* **28**(12), 123602 (2016).

<sup>2</sup>J. J. Murray, A. Guha, and A. Bond, "Overview of the development of heat exchangers for use in air-breathing propulsion pre-coolers," *Acta Astronaut.* **41**(11), 723–729 (1997).

<sup>3</sup>W. R. Dean, "The stream-line motion of fluid in a curved pipe," *London, Edinburgh, Dublin Philos. Mag. J. Sci.* **5**(30), 673–695 (1928).

<sup>4</sup>A. Guha, "A unified Eulerian theory of turbulent deposition to smooth and rough surfaces," *J. Aerosol Sci.* **28**(8), 1517–1537 (1997).

<sup>5</sup>A. Guha, "Transport and deposition of particles in turbulent and laminar flow," *Annu. Rev. Fluid Mech.* **40**, 311–341 (2008).

<sup>6</sup>J. H. Horlock, "Some experiments on the secondary flow in pipe bends," *Proc. R. Soc. London, Ser. A* **234**, 335–346 (1956).

<sup>7</sup>W. R. Hawthorne, "The growth of secondary circulation in frictionless flow," *Math. Proc. Cambridge Philos. Soc.* **51**, 737–743 (1955).

<sup>8</sup>R. W. Detra, "The secondary flow in curved pipes," D.Sc. thesis, The Swiss Federal Institute of Technology, Zurich, 1953.

<sup>9</sup>M. Rowe, "Measurements and computations of flow in pipe bends," *J. Fluid Mech.* **43**(4), 771–783 (1970).

<sup>10</sup>Y. Agrawal, L. Talbot, and K. Gong, "Laser anemometer study of flow development in curved circular pipes," *J. Fluid Mech.* **85**(3), 497–518 (1978).

<sup>11</sup>S. Dey, "Secondary boundary layer and wall shear for fully developed flow in curved pipes," *Proc. R. Soc. London, Ser. A* **458**, 283–298 (2002).

<sup>12</sup>S. A. Berger, L. Talbot, and L. S. Yao, "Flow in curved pipes," *Annu. Rev. Fluid Mech.* **15**, 461–512 (1983).

<sup>13</sup>W. R. Dean, "Fluid motion in a curved channel," *Proc. R. Soc. London, Ser. A* **121**, 402–420 (1928).

<sup>14</sup>S. N. Barua, "On secondary flow in stationary curved pipes," *Q. J. Mech. Appl. Math.* **16**(1), 61–77 (1963).

<sup>15</sup>L. Talbot and K. O. Gong, "Pulsatile entrance flow in a curved pipe," *J. Fluid Mech.* **127**, 1–25 (1983).

<sup>16</sup>Y. Zhao and B. B. Lieber, "Steady inspiratory flow in a model symmetric bifurcation," *J. Biomech. Eng.* **116**(4), 488–496 (1994).

<sup>17</sup>Y. Zhao and B. B. Lieber, "Steady expiratory flow in a model symmetric bifurcation," *J. Biomech. Eng.* **116**(3), 318–323 (1994).

<sup>18</sup>P. Evengren, L. Fuchs, and J. Revstedt, "On the secondary flow through bifurcating pipes," *Phys. Fluids* **22**(10), 103601 (2010).

<sup>19</sup>F. Y. Leong, K. A. Smith, and C. H. Wang, "Secondary flow behavior in a double bifurcation," *Phys. Fluids* **21**(4), 043601 (2009).

<sup>20</sup>F. E. Fresconi and A. K. Prasad, "Secondary velocity fields in the conducting airways of the human lung," *J. Biomech. Eng.* **129**(5), 722–732 (2007).

<sup>21</sup>E. R. Weibel, "Geometric and dimensional airway models of conductive, transitory and respiratory zones of the human lung," in *Morphometry of the Human Lung* (Springer, Berlin, Heidelberg, 1963), pp. 136–142.

<sup>22</sup>SolidWorks, Release 2010, Dassault Systèmes SolidWorks Corporation, Waltham, USA.

<sup>23</sup>ANSYS Academic Research, Release 15.0, ANSYS, Inc., Canonsburg, USA.

<sup>24</sup>P. W. Longest and S. Vinchurkar, "Effects of mesh style and grid convergence on particle deposition in bifurcating airway models with comparisons to experimental data," *Med. Eng. Phys.* **29**(3), 350–366 (2007).

<sup>25</sup>J. K. Comer, C. Kleinstreuer, and Z. Zhang, "Flow structures and particle deposition patterns in double-bifurcation airway models. Part 1. Air flow fields," *J. Fluid Mech.* **435**, 25–54 (2001).

<sup>26</sup>N. Nowak, P. P. Kakade, and A. V. Annapragada, "Computational fluid dynamics simulation of airflow and aerosol deposition in human lungs," *Ann. Biomed. Eng.* **31**(4), 374–390 (2003).

<sup>27</sup>T. J. Barth and D. C. Jespersen, "The design and application of upwind schemes on unstructured meshes," AIAA Paper No. 89-0366, 1989.

<sup>28</sup>Y. Mei and A. Guha, "Implicit numerical simulation of transonic flow through turbine cascades on unstructured grids," *Proc. Inst. Mech. Eng., Part A* **219**(1), 35–47 (2005).

<sup>29</sup>A. Guha and J. B. Young, "Time-marching prediction of unsteady condensation phenomena due to supercritical heat addition," in *Turbomachinery: Latest Developments in a Changing Scene* (Institution of Mechanical Engineers, London, UK, 1991), ISBN: 0852987617.

<sup>30</sup>A. Guha, "Thermal choking due to nonequilibrium condensation," *J. Fluids Eng.* **116**(3), 599–604 (1994).

<sup>31</sup>M. Y. Kang, J. Hwang, and J. W. Lee, "Effect of geometric variations on pressure loss for a model bifurcation of the human lung airway," *J. Biomech.* **44**(6), 1196–1199 (2011).

<sup>32</sup>C. H. Zhang, Y. Liu, R. M. C. So, and N. Phan-Thien, "The influence of inlet velocity profile on three-dimensional three-generation bifurcating flows," *Comput. Mech.* **29**(4-5), 422–429 (2002).

<sup>33</sup>Y. Liu, R. M. C. So, and C. H. Zhang, "Modeling the bifurcating flow in a human lung airway," *J. Biomech.* **35**(4), 465–473 (2002).

<sup>34</sup>P. J. Roache, "Quantification of uncertainty in computational fluid dynamics," *Annu. Rev. Fluid Mech.* **29**, 123–160 (1997).

<sup>35</sup>A. Moskal and L. Gradoń, "Temporary and spatial deposition of aerosol particles in the upper human airways during breathing cycle," *J. Aerosol Sci.* **33**(11), 1525–1539 (2002).

<sup>36</sup>J. Jeong and F. Hussain, "On the identification of a vortex," *J. Fluid Mech.* **285**, 69–94 (1995).